Journal of Power Sources 667 (2026) 239111

Contents lists available at ScienceDirect

Journal of Power Sources

journal homepage: www.elsevier.com/locate/jpowsour

Practical considerations and limitations of online EIS-based battery internal temperature estimation in traction applications

Norbert Sailer [a,b,*], Christoph Steffan [b], Jan Philipp Schmidt [a]

[a] Chair of Systems Engineering for Electrical Energy Storage (SysEE), Bavarian Center for Battery Technology (BayBatt), University of Bayreuth, Universitätsstraße 30, Bayreuth, 95447, Bavaria, Germany

[b] Infineon Technologies Austria AG, Babenbergerstraße 10, 8020 Graz, Austria

HIGHLIGHTS

- Meta–analysis of 68 publications comprising 83 cells.
- Impedance phase effectively estimates internal cell temperature.
- Optimal frequency range: 100 Hz to 1 kHz.
- Mean sensitivity of $-0.17\,^{\circ}\,K^{-1}$ for $T > 23\,^{\circ}C$.
- EV traction inverter noise might impact EIS up to 3 kHz.

ARTICLE INFO

Dataset link: https://doi.org/10.17632/zdpxdkx6rn.1, https://doi.org/10.17632/562fxrn7js.1

Keywords:
Electrochemical Impedance Spectroscopy (EIS)
Internal temperature estimation
Battery Management System (BMS)

ABSTRACT

Based on a meta–analysis of 68 publications comprising 83 cells, extended by our own measurements, we propose the impedance phase, evaluated at frequencies between 100 Hz and 1 kHz, as an optimal estimator for internal cell temperature. Our findings indicate mean temperature sensitivities of $-0.35\,^{\circ}\,K^{-1}$ for temperatures below 23 °C and $-0.17\,^{\circ}\,K^{-1}$ for temperatures above 23 °C. Notably, these sensitivities remain constant regardless of the cell's capacity and chemistry. To achieve a temperature uncertainty of less than 1 K for high-energy cells above 23 °C, an Electrochemical Impedance Spectroscopy (EIS) measurement system must maintain an uncertainty smaller than 4 μΩ for both the real and imaginary components of the impedance, based on the mean sensitivities. In addition to the electrochemical properties of the cells, system characteristics of the application must also be considered for online temperature estimation. Our proposed noise model for traction applications in general, and measurement results for an Electric Vehicle (EV) specifically, demonstrate that disturbances with significant power may disturb online EIS measurements up to 3 kHz.

1. Introduction

Battery-powered systems rely on a Battery Management System (BMS) to estimate the battery state, ensuring that the system operates within safe operating limits while optimizing battery performance. The accuracy with which the BMS estimates the battery states directly influences the safety and performance of the battery–powered system. Current state–of–the–art BMSs measure the battery current, individual cell voltages, and battery pack surface temperatures [1]. These measurements may be processed using an electro-thermal battery model to determine battery states, such as State of Charge (SoC), State of Health (SoH), and the minimum, maximum, and internal cell temperatures.

During battery operation, the temperature distribution within the cell is often inhomogeneous, leading to substantial temperature gradients between the core and the surface of the cell [2–11]. For instance, Zhang et al. applied 3 C charge and discharge pulses to a prismatic 10 Ah cell at ambient temperatures of 26 °C and 5 °C, measuring a temperature difference of 6 K and 10 K between the internal and surface temperature, respectively [7]. Similarly, a temperature difference of 20 K was measured during a 50 C discharge of a prismatic 20 Ah cell at 25 °C ambient temperature [3]. Comparable temperature gradients have also been observed in cylindrical and pouch cells. During 1 C constant current charging and discharging cycles at 20 °C, Bhoir et al. measured temperature differences of up to 12 K using a 12 Ah

* Corresponding author at: Chair of Systems Engineering for Electrical Energy Storage (SysEE), Bavarian Center for Battery Technology (BayBatt), University of Bayreuth, Universitätsstraße 30, Bayreuth, 95447, Bavaria, Germany.
E-mail addresses: norbert.sailer@uni-bayreuth.de (N. Sailer), christoph.steffan@infineon.com (C. Steffan), jan.schmidt@uni-bayreuth.de (J.P. Schmidt).

https://doi.org/10.1016/j.jpowsour.2025.239111
Received 20 October 2025; Received in revised form 3 December 2025; Accepted 12 December 2025
Available online 13 January 2026

Nomenclature

Acronyms

$\mathcal{Z}$	Impedance feature
BMS	Battery Management System
EIS	Electrochemical Impedance Spectroscopy
ENBW	Equivalent Noise Bandwidth
EV	Electric Vehicle
G	Graphite
GSi	Graphite and Silicon
HC	Hard Carbon
IQR	Interquartile Range
LCO	Lithium Ion Cobalt Oxide
LFP	Lithium Ion Phosphate
LiPo	Lithium Ion Polymer
LMO	Lithium Ion Manganese Oxide
LTO	Lithium Ion Titanium Oxide
NaLO	Natrium Layered Oxide
NCA	Lithium Ion Nickel Cobalt Aluminum Oxide
NMC	Lithium Ion Nickel Manganese Cobalt Oxide
PSD	Power Spectral Density
PWM	Pulse–Width Modulation
SEI	Solid Electrolyte Interphase
SIB	Sodium Ion Battery
SoC	State of Charge
SoH	State of Health
STFT	Short–Time Fourier transform

Variables

$\mathrm{abs}(Z)$	Absolute value of impedance Ω
$\arg(Z)$	Impedance phase °
f_{arc}	Characteristic arc frequency Hz
f_{t}	Transition frequency Hz
f_{el}	Electric motor control signal Hz
f_{int}	Intercept frequency Hz
f_{rot}	Mechanical motor rotational frequency Hz
f_{sw}	Switching frequency of traction inverter Hz
$\mathrm{Im}(Z)$	Imaginary part of impedance Ω
N_{P}	Number of pole pairs
$\mathrm{Re}(Z)$	Real part of impedance Ω
$\alpha_{\mathrm{int/arc}}$	High–frequency ratio
$\alpha_{\mathrm{arc/t}}$	Low–frequency ratio
σ	Standard deviation
$S_{\mathcal{Z},\mathrm{T\,n}}$	Normalized sensitivity of impedance feature with respect to temperature $\%\,\mathrm{K}^{-1}$
$S_{\mathcal{Z},\mathrm{T}}$	Sensitivity of impedance feature with respect to temperature
T_{int}	Internal cell temperature °C
f	Frequency Hz
Q	Cell capacity Ah
T	Temperature °C

pouch cell [2]. Furthermore, constant current charge and discharge experiments on cylindrical cells at 1 C and 3 C exhibited temperature differences ranging from 3 K to 10 K [4,5,9]. Forced convection increased the temperature difference from 3 K to 5.5 K during a 3 C discharge [9]. Richardson et al. measured a temperature difference of up to 8 K in 26 650 cylindrical cells at an ambient temperature of 8 °C, while applying Electric Vehicle (EV) drive profiles with currents reaching 13 C [6,10].

In addition to the temperature gradients measured between internal and surface temperatures, significant temperature variations occur along the surface and within planes inside the cell [3,5–7,10,12]. During the aforementioned EV drive profile experiment, Richardson et al. measured a temperature difference of up to 3 K across the surface of the cylindrical cell [6]. Yu et al. utilized an optical fiber to measure the temperature distribution along a 21 700 cylindrical cell during a 1 C discharge and charge cycle at 25 °C, revealing temperature variations of 7 K to 10 K along the internal and external fibers, respectively [5]. Temperature differences of 8 K and 10 K were measured inside and at the surface of a 20 Ah prismatic cell while discharging with 60 C current pulses at 25 °C [3]. Using infrared imaging, Veth et al. reported a surface temperature difference of up to 9 K on a 50 Ah pouch cell during a 6 C constant current discharge [12].

The temperature differences observed between sensors placed inside the cell and those along the surface, as well as gradients within the cell and along its surface, have been reported across cylindrical, pouch, and prismatic cells under application-like operating conditions. The main difference in the thermal behavior between cell types is their difference in surface–area–to–volume ratio [8]. The reported temperature gradients tend to increase with higher current rates and lower cell temperatures, primarily due to higher Joule losses. The implementation of forced cooling on the cell surface may increase the observed temperature differences. Consequently, internal cell temperature serves as a more accurate indicator of the cell's maximum temperature compared to surface-mounted sensors, particularly under abnormal operating conditions.

Accurately determining the internal cell temperature can enhance battery temperature control, facilitating the optimization of temperature settings for fast charging and maximizing cycle life [13–15]. Additionally, it can enable earlier detection of abnormal operating conditions that lead to thermal runaway compared to cell voltage and surface temperature measurements [16–18].

Srinivasan et al. [19] used EIS to estimate the internal cell temperature T_{int}. An impedance feature $\mathcal{Z}$ measured at a specific frequency f, the impedance phase at 40 Hz in the cited study, correlates with T_{int}. Thus, the internal cell temperature can be expressed as

$$T_{\mathrm{int}} = g\left(\mathcal{Z}(f)\right), \tag{1}$$

where $g()$ denotes a fitted model characterizing the relationship between the internal cell temperature and the impedance feature. The temperature estimated by EIS corresponds to the mean internal cell temperature [11,20].

The dependence of a cell's impedance on SoC, SoH, and temperature under laboratory conditions is well researched [21–29]. Laboratory conditions imply that the cell is in both electrochemical and thermal equilibrium, free from application influences, and measured using high-precision equipment. However, when EIS is used for online battery state estimation in EVs, noise during EIS measurements may introduce errors in the impedance results and consequently in internal cell temperature estimates. Furthermore, the impedance measurement capabilities of the BMS might not achieve the level of accuracy seen with laboratory measurement equipment. Raijmakers et al. found that the battery pack current of an EV contains spectral components with magnitudes in the range of 10 mA to 100 mA for frequencies between 100 Hz and 400 Hz [30]. Above 1 kHz, powertrain noise decreased by about a factor of ten, reaching the mA range. The frequency range of powertrain noise, which contains sufficient energy for interferences, overlaps with the EIS measurement frequency range. To mitigate interferences during online EIS in EVs, Raijmakers et al. recommend choosing measurement frequencies above 1 kHz.

In our opinion, previous studies on EIS–based internal cell temperature estimation are unsatisfactory for three reasons:

(1) While individual studies have identified optimal EIS parameters for their specific cells, no impedance feature and measurement frequency range, independent of cell capacity and chemistry, have been established [31–33]. Investigations by Zheng et al. [34] and Hackmann et al. [22] have proposed using the impedance phase and the imaginary part of the impedance measured at frequencies corresponding to the Solid Electrolyte Interphase (SEI) layer [35–38]. However, they do not specify a particular frequency range that could guide practical implementation. The fundamental question of whether universally applicable impedance features and frequency ranges exist across diverse cell chemistries, form factors, and capacities remain unanswered.

(2) The sensitivities of impedance features with respect to temperature remain unreported. Therefore, proposed estimators cannot be effectively compared and the necessary measurement accuracy for an impedance measurement function within a BMS cannot be established.

(3) Impedance characterizations and temperature estimator validations have primarily been conducted under laboratory conditions, with the exception of Raijmakers et al. [30]. For accurate and reliable online estimator performance, application-specific noise that might interfere with the EIS measurement should be accounted for when selecting impedance feature and measurement frequency.

These considerations extend beyond EIS–based internal cell temperature estimation, as they are equally important for all EIS–based battery state estimators, including SoC [39] and SoH [21,40–43].

Through our methodology (Section 2) and subsequent analysis (Section 4), we conduct a meta–analysis of 68 publications comprising 83 cells and their respective impedance datasets to systematically identify a universally applicable impedance feature and measurement frequency range for internal cell temperature estimation. We propose a systematic analysis scheme that quantifies impedance sensitivities with respect to temperature, yielding sensitivity coefficients in units of $\Omega\,K^{-1}$, $^\circ K^{-1}$, or $Hz\,K^{-1}$, depending on the specific impedance feature used. This framework enables direct quantitative comparison of internal cell temperature estimators across different studies and cell types. Furthermore, our framework facilitates the derivation of measurement accuracy requirements for EIS–based BMS functions, providing design criteria for practical BMSs.

We extended the test-bench characterization of EV powertrain noise conducted by Raijmakers et al. [30] to real-world drive profiles in Sections 2 and 5. In addition to presenting these measurement results, we provide a simplified EV powertrain noise model to assess whether the findings from Section 4, based on electrochemical cell behavior, can be effectively applied in real–world scenarios.

2. Methods

To identify the optimal impedance feature and measurement frequency range for estimating internal cell temperature, we compiled two datasets from existing studies and our experimental data. Our experimental procedures and setups are detailed in Section 3. The two datasets contain measurement data of commercial cells with established cell form factors, including cylindrical, pouch, and prismatic cells, as well as established cell chemistries such as Lithium Ion Phosphate (LFP), Lithium Ion Nickel Cobalt Aluminum Oxide (NCA), Lithium Ion Nickel Manganese Cobalt Oxide (NMC), and more recent developments like Sodium Ion Batterys (SIBs).

The first dataset, referred to as ***Dataset A*** [44], includes the measured temperature dependence of impedance features $\mathcal{Z}$, evaluated at frequency f as a function of cell temperature, specifically proposed for internal cell temperature estimation. This dataset contains impedance-temperature data from 86 estimators, only including studies that use either the real part $\mathrm{Re}(Z)$, the imaginary part $\mathrm{Im}(Z)$, the absolute value $\mathrm{abs}(Z)$ of the impedance, or the impedance phase $\arg(Z)$. These features are measured at a single-frequency. In contrast, the intercept frequency f_{int}, defined as the frequency where the imaginary part of the impedance equals zero ($f_{\mathrm{int}} := \mathrm{Im}(Z(f)) = 0$) requires a frequency sweep to be determined [27]. We included f_{int} as the only multi-frequency impedance feature. Using Dataset A, we aim to determine the optimal impedance feature for internal cell temperature estimation.

The second dataset, ***Dataset B*** [44], contains EIS measurement data, which includes the real and imaginary part of the impedance and the measurement frequency. To facilitate comparison of impedance across different cells, we focused on data measured at 50% SoC, 100% SoH, and 23 °C or the closest available operating point. This approach enables us to identify the frequency range of the SEI layer for various cell types, capacities, and chemistries. Dataset B contains 44 cells, with 12 of these also included in Dataset A.

2.1. Dataset A: Evaluating temperature sensitivity in impedance features

We analyzed 49 publications containing impedance–temperature data from 86 estimators. A summary of these studies is provided in Table A.1, detailing the impedance feature $\mathcal{Z}$, measurement frequency f, impedance sensitivities regarding temperature $S_{\mathcal{Z},\mathrm{T}}$, cell capacity Q, and negative/positive electrode active materials.

The impedance phase $\arg(Z)$ is the most frequently used feature for temperature estimation, appearing in 50 instances (58%), followed by the imaginary part $\mathrm{Im}(Z)$ (12 instances; 14%). Other impedance features include the absolute value $\mathrm{abs}(Z)$ (11 instances; 13%), the real part $\mathrm{Re}(Z)$ (8 instances; 9%), and the intercept frequency f_{int} (5 instances; 6%). The majority of the studies focus on cylindrical cells (55 instances; 64%) and low-capacity cells with capacities below 5 Ah (58 instances; 58%). The dataset presents a balanced distribution of positive electrode active materials among LFP, NCA, and NMC. A visual summary of these metadata is shown in Fig. 2.

To identify the optimal impedance feature for internal cell temperature estimation, we employed a systematic analysis scheme. First, for each publication listed in Table A.1, we extracted the measured temperature dependence of the impedance feature $\mathcal{Z}$ as described by Eq. (1). Whenever possible, we used the experimental data or fitting function provided by the authors. In instances where no equation was available, we used the WebPlotDigitizer tool [45,46] to extract data from the plots. Second, the extracted data were fitted with linear, exponential, and second–degree polynomial functions to ensure consistency in processing and interpolating data points. The best fit was determined based on the R^2 value. Third, the sensitivities of the impedance feature with respect to temperature, denoted as $S_{\mathcal{Z},\mathrm{T}}$, were calculated. These calculations were performed by linearly interpolating between the minimum temperature and 23 °C, and between 23 °C and the maximum temperature, yielding $S_{\mathcal{Z},\mathrm{T}_1}$ and $S_{\mathcal{Z},\mathrm{T}_2}$, respectively. To maintain comparability, we limited the temperature range for this calculation from −20 °C to 60 °C. Finally, we calculated the normalized sensitivities of the impedance feature regarding temperature, denoted as $S_{\mathcal{Z},\mathrm{T\,n}}$, in $\%\,K^{-1}$ by dividing $S_{\mathcal{Z},\mathrm{T}}$ by the value of the impedance feature at 23 °C ($\mathcal{Z}_{23\,^\circ\mathrm{C}}$):

$$S_{\mathcal{Z},\mathrm{T\,n}} = \frac{S_{\mathcal{Z},\mathrm{T}}}{\mathcal{Z}_{23\,^\circ\mathrm{C}}} \cdot 100\% \tag{2}$$

The normalized sensitivity $S_{\mathcal{Z},\mathrm{T\,n}}$ facilitates comparison across all impedance features, regardless of units and cell properties.

This process is exemplified for an LG INR18650 MJ1 3.5 Ah cell (Cell A) in Fig. 1. The negative impedance phase, measured at 1 kHz, decreases with increasing temperature. The impedance phase-temperature sensitivity $S_{-\arg(Z),\mathrm{T}}$ also decreases with increasing temperature, being $-0.21\,^\circ\,K^{-1}$ for temperatures below 23 °C and $-0.13\,^\circ\,K^{-1}$ for temperatures above 23 °C. The impedance phase value at 23 °C is $\mathcal{Z}_{23\,^\circ\mathrm{C}} = -2.72°$. Normalizing $S_{-\arg(Z),\mathrm{T}}$ by $\mathcal{Z}_{23\,^\circ\mathrm{C}}$ yields 7.86 %K and 4.85 %K for the low and high temperature range, respectively.

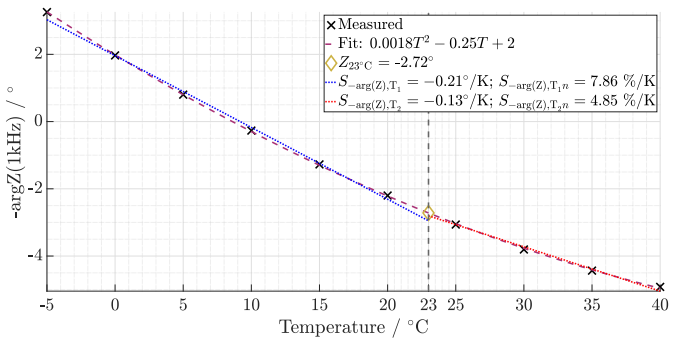

Fig. 1. Negative impedance phase $-\arg(Z)$ measured at 1 kHz of a 3.5 Ah LG INR18650 MJ1 cell (Cell A) as a function of temperature at 50% State of Charge (SoC). The black crosses represent the measured data, while the dashed lines represent the data fitted to a second–degree polynomial ($-\arg(Z(1\,\text{kHz})) = 0.0018T^2 - 0.25T + 2$). Interpolating the fitted data linearly for temperatures below and above 23 °C yields the impedance phase–temperature sensitivities $S_{-\arg(Z),T_1} = -0.21\,°\,\text{K}^{-1}$ and $S_{-\arg(Z),T_2} = -0.13\,°\,\text{K}^{-1}$. The normalized sensitivities $S_{-\arg(Z),T\,n}$, defined as the ratio of $S_{-\arg(Z),T}$ and the value of the impedance feature at 23 °C ($Z_{23\,°C}$), are 7.86 %K and 4.85 %K for the two temperature regions, respectively.

2.2. Dataset B: Determining optimal measurement frequency

We compiled a dataset from existing studies and our experimental data, containing the real and imaginary parts of the impedance, along with the measurement frequency of 44 cells to identify the optimal measurement frequency range for estimating the internal cell temperature using EIS. The cells were characterized at 50% SoC, 100% SoH, and 23 °C or the closest available operating point. A summary of the operating points, cell properties, and data sources is provided in Table B.1. Of the 44 cells, 12 cells are included in Dataset A (Table A.1). Dataset B predominantly consists of data from cylindrical cells (28 instances; 64%) and low–capacity cells with capacities below 5 Ah (28 instances; 64%), as illustrated in the metadata visual summary in Fig. 2.

For each cell, we extracted five features from the Nyquist curves:

- Intercept frequency $f_{\text{int}} := \text{Im}(Z(f)) = 0$; ohmic impedance, marking the transition point between capacitive and inductive behavior.
- Characteristic frequency of the arc $f_{\text{arc}} := \max(\text{Im}(Z(f)))$; the frequency at which the imaginary part of the impedance reaches its maximum within the semicircle, satisfying the condition $f_{\text{int}} > f_{\text{arc}} > f_{\text{t}}$.
- Transition frequency $f_{\text{t}} := \min(\text{Im}(Z(f)))$; the frequency where the imaginary part of the impedance reaches its minimum for values lower than the characteristic arc frequency f_{arc}, marking the transition point between the semicircle and the diffusion tail.
- Low–frequency ratio $\alpha_{\text{arc/t}} := \frac{f_{\text{arc}}}{f_{\text{t}}}$
- High–frequency ratio $\alpha_{\text{int/arc}} := \frac{f_{\text{int}}}{f_{\text{arc}}}$

The three features in the Nyquist plot are highlighted in Fig. 3 for a 3.5 Ah cylindrical cell (Cell A) and a 75 Ah prismatic cell (Cell F). For comparison, the Nyquist curves are normalized with respect to the maximum absolute value of the real and imaginary components of each cell. The data is limited to a frequency range between 2 kHz and 100 mHz. The characteristic arc and the transition frequency are nearly equivalent for both cells. However, the intercept frequency of the cylindrical cell is approximately 3.3 times greater than that of the prismatic cell. This difference can be attributed to the generally higher impedance characteristic of the cylindrical cell. Identical inductance values added would lead to a higher intercept frequency for the cylindrical cell compared to the prismatic cell.

3. Experimental

In this study, we conducted two complementary experimental investigations: (1) systematic EIS characterization of cells as a function of temperature under controlled laboratory conditions, and (2) real–world EV traction current measurements to capture the actual charge and discharge conditions experienced by batteries in EVs.

3.1. Cell impedance–temperature characterization

We measured the impedance of six different cells (designated A through F) across various temperature ranges, as detailed in Table 1. Our test matrix includes cells with different chemistries (LFP, NMC, and SIB), form factors (cylindrical and prismatic), and capacity ratings ranging from 1.2 Ah to 75 Ah.

All cells were pristine except Cell A, which was extracted from an electric bicycle battery pack with unknown cycling history. Its measured remaining capacity was 90% of the nominal cell capacity. All measurements were conducted at 50% SoC.

Charging, discharging, and EIS were performed using BioLogic SP-300 [47] and VMP-300 [48] electrochemical workstations, with the exception of Cell A, which was characterized using a custom EIS measurement system [49]. The temperature was controlled through environmental chambers (CTS T65-50 [50] and Vötsch VTS 7011-5) providing indirect ambient temperature control, except for Cell A, where direct surface control was implemented using a custom-built thermal management system.

EIS measurements employed sinusoidal excitation currents with logarithmic frequency spacing of at least four points per decade, covering the frequency range from 20 kHz to 100 mHz. Peak excitation current amplitudes were optimized for each cell to ensure linear response while maintaining adequate signal–to–noise ratio, as specified in Table 1.

Prior to impedance characterization, each cell underwent five charge–discharge cycles at 35 °C using constant current–constant voltage (CC–CV) charging and constant current (CC) discharging according to manufacturer specifications.

The experimental procedure for measuring impedance as a function of temperature for each cell was carried out according to the following steps:

1. Cells were maintained at 35 °C for 3 h to ensure uniform temperature distribution throughout the cell structure.
2. Set SoC: Cells were charged to 100% SoC using CC–CV protocol, then discharged to 50% SoC using CC–CV according to manufacturer specifications. A minimum rest period of 12 h was implemented to achieve electrochemical equilibrium.
3. Set temperature: Target temperature was set with 3 h stabilization time to ensure thermal equilibrium throughout the cell.
4. EIS was performed according to the parameters in Table 1 followed by a 1 h rest period.
5. Measurements progressed in 5 °C steps within specified ranges, starting from the highest temperature (step 3).

Our experimental data, along with postprocessing scripts, is available as a dataset [44].

3.2. EV traction current measurement

Real-world battery current characterization was performed using a Citroën C-Zero equipped with a battery pack consisting of 88 cells connected in series. Each cell has a nominal capacity of 50 Ah.

Current measurements were acquired using a Hioki 3275 current clamp [51] with 2 MHz bandwidth, connected on the positive high-voltage cable at the traction inverter input. The current clamp output signal was digitized using a PicoScope 5444D oscilloscope [52] at sample frequencies ranging from 50 kHz to 20 MHz. We evaluated six representative driving scenarios to capture a wide spectrum of EV operating conditions:

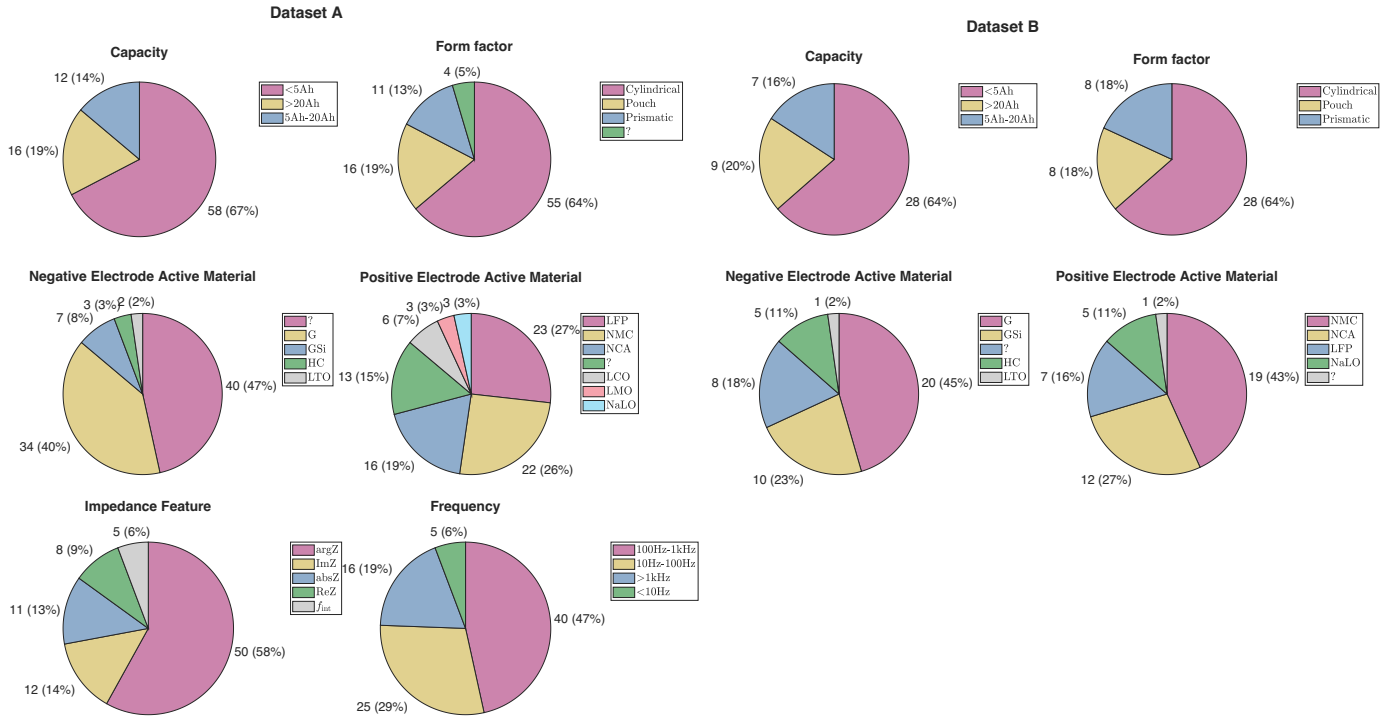

Fig. 2. Visual summaries of the metadata of the analyzed Electrochemical Impedance Spectroscopy (EIS) internal cell temperature estimators of Dataset A listed in Table A.1 [44], and of the EIS data of Dataset B listed in Table B.1 [44]. **Left**: ***Dataset A*** – The 49 publications investigated 86 estimators. The most frequently used impedance feature used for internal cell temperature estimation is the impedance phase $\arg(Z)$ (50 instances; 58%) followed by the imaginary part of the impedance $\mathrm{Im}(Z)$ (12 instances; 14%). Researchers predominantly use cylindrical cells (55 instances; 64%) and low–capacity cells below 5 Ah (58 instances; 67%). The dataset presents a balanced distribution of positive electrode active materials among Lithium Ion Phosphate (LFP), Lithium Ion Nickel Cobalt Aluminum Oxide (NCA), and Lithium Ion Nickel Manganese Cobalt Oxide (NMC). **Right**: ***Dataset B*** – This dataset includes 44 cells. Researchers predominantly use cylindrical cells (28 instances; 64%) and low–capacity cells below 5 Ah (28 instances; 64%). 12 cells are contained in both datasets and together they contain data of 83 cells.

Table 1
Overview of cells, experimental devices, and parameters used in this study. The cell's nominal capacity Q is presented in Ah, along with the negative/positive electrode active materials (Neg/Pos). Operational parameters, such as State of Charge (SoC), State of Health (SoH), minimum temperature T_{min}, maximum temperature T_{max}, and temperature steps ΔT, are also included. Additionally, the peak amplitude of the sinusoidal Electrochemical Impedance Spectroscopy (EIS) excitation current (i_{exc}) and maximum and minimum frequencies of the frequency sweep are documented.

Cell									Experimental Setup				
	Q	Form factor	Neg/Pos	SoC	SoH	T_{min}	T_{max}	ΔT	EIS	i_{exc}	f_{max}	f_{min}	T
	Ah			%	%	°C	°C	°C		C	kHz	Hz	
A[a]	3.5	Cylindrical	GSi/NMC	50	90	−5	40	5	I	0.14	20	0.1	IV
B[b]	1.2	Cylindrical	G/LFP	50	100	5	35	5	II	0.42	20	0.1	V
C[c]	1.3	Cylindrical	HC/NaLO	50	100	−5	50	5	III	0.38	20	0.1	VI
D[d]	4.5	Cylindrical	GSi/NMC	50	100	0	45	5	III	0.22	20	0.1	VI
E[e]	3.5	Cylindrical	GSi/NMC	50	100	0	50	5	II	0.14	20	0.1	V
F[f]	75	Prismatic	G/NMC	50	100	0	45	5	III	0.15	20	0.1	VI

[a]	LG Chem	MJ1	I: Custom [49]
[b]	LithiumWerks	APR18650M1B	II: BioLogic SP-300 [47]
[c]	Shenzhen Zhonghuajia Technology Co.,Ltd.	18 650–1300 mAh	III: BioLogic VMP-300 [48]
[d]	Molicel	INR21700-P45B	IV: Custom
[e]	Molicel	INR18650-M35A	V: CTS T65-50 [50]
[f]	Westart	PHEV-75 Ah	VI: Vötsch VTS 7011-5

1. Parking mode: Vehicle stationary with auxiliary systems active
2. Acceleration: High acceleration from standstill to approximately 50 km h^{-1}
3. Regenerative breaking: Controlled deceleration from approximately 50 km h^{-1} to standstill
4. Constant velocity: Steady-state driving at approximately 25 km h^{-1}
5. Urban driving: Moderate acceleration and deceleration patterns
6. Dynamic driving: High-performance driving with rapid acceleration and deceleration

Time–frequency analysis of the current signals was performed using Short–Time Fourier transform (STFT) to characterize the spectral components during different driving scenarios.

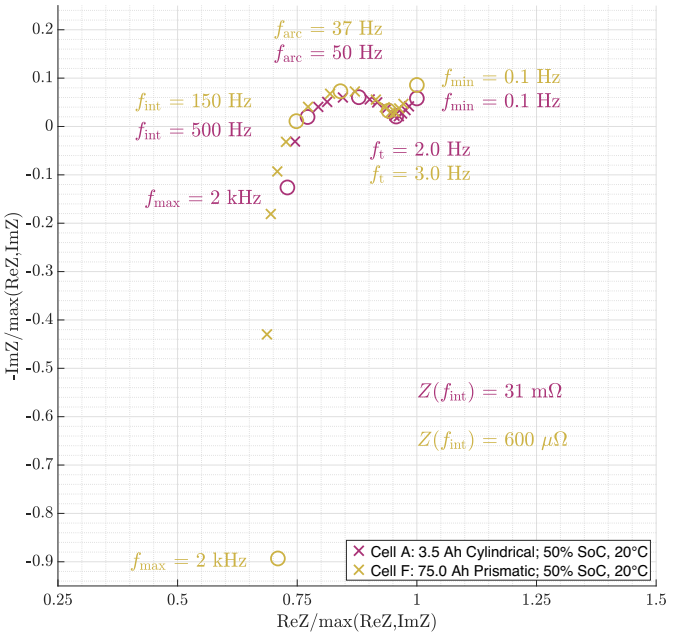

Fig. 3. Normalized Nyquist curves of a 3.5 Ah cylindrical cell (Cell A) and a 75 Ah prismatic cell (Cell F). The impedances are normalized with respect to the maximum absolute value of the real and imaginary components of each cell. The measurement frequency ranges from 2 kHz to 100 mHz. The characteristic arc frequency f_{arc} and the transition frequency f_t are nearly equivalent for both cells. In contrast, the intercept frequency of the cylindrical cell is about 3.3 times higher than that of the prismatic cell.

Our experimental data, along with postprocessing scripts, is available as a dataset [53].

4. Results and discussion – Optimal impedance feature and frequency selection

This section presents our analysis results of Dataset A and Dataset B. We first evaluate the temperature sensitivity of different impedance features across various cell types and capacities to identify the optimal impedance feature for internal cell temperature estimation (Section 4.1). Subsequently, in Section 4.2, we analyze impedance spectra to identify the frequency range of the SEI layer. Finally, we translate these findings into practical design criteria by establishing accuracy requirements for EIS–enabled BMSs (Section 4.3).

4.1. Dataset A: Evaluating temperature sensitivity in impedance features

To identify the optimal impedance feature, we plotted the calculated sensitivities $S_{\mathcal{Z},T}$ against cell capacity Q and measurement frequency f for each impedance feature. The results for the negative impedance phase $-\arg(Z)$ are illustrated in Fig. 4. Notably, $S_{-\arg(Z),T}$ increases with increasing cell capacity. Conversely, $S_{-\arg(Z),T}$ decreases with increasing temperature and measurement frequency.

Plots for all other impedance features are included in Section S1 of the supplementary material linked in Appendix D. A summary of the results is presented in Table 2, which demonstrates that the impedance phase is the only impedance feature whose sensitivity regarding temperature increases with increasing capacity. All other impedance features exhibit reduced sensitivity with larger capacities. This observation aligns with the findings of Srinivasan et al. [54], who noted that the phase's sensitivity to temperature is less affected by changes in cell capacity compared to other impedance features. Additionally, at higher temperatures and the measurement frequencies, the sensitivity decreases. This trend is consistent across all impedance features as charge-transfer and diffusion processes show an exponential dependence on temperature. At higher frequencies, these processes influence impedance less, as they dominate at frequencies below 100 Hz.

Table 2
Behavior of impedance feature $\mathcal{Z}$ as the cell temperature increases (T ↗) and the sensitivity of the impedance feature regarding temperature $S_{\mathcal{Z},T}$ with rising cell temperature (T ↗), cell capacity (Q ↗), and measurement frequency (f ↗). Notably, the impedance phase $\arg(Z)$ is the only impedance feature that increases with increasing cell capacity. As temperature and measurement frequency rise, the sensitivity $S_{\mathcal{Z},T}$ decreases. The table also indicates the number of cells (No.) corresponding to each $\mathcal{Z}$ in Dataset A, which is summarized in Table A.1.

$\mathcal{Z}$	No.	T ↗	$S_{\mathcal{Z},T}$ (T ↗)	$S_{\mathcal{Z},T}$ (Q ↗)	$S_{\mathcal{Z},T}$ (f ↗)
$\mathrm{Re}(Z)$	8	↘	↘	↘[a]	↘[a]
$-\mathrm{Im}(Z)$	12	↘	↘	↘	↘
$\mathrm{abs}(Z)$	11	↘	↘	↘	↘[b]
$-\arg(Z)$	50	↘	↘	↗	↘
f_{int}	5	↘	↘	↘	–

[a] According to Schmidt et al. [11], with no clear correlation evident in our dataset.
[b] $\mathrm{abs}(Z)$ and $\mathrm{Re}(Z)$ exhibit same dependency on Q and f, with no clear correlation evident in our dataset.

A more detailed analysis of the dataset is presented in Table 3, categorizing the data into three cell form factors: cylindrical, pouch, and prismatic cells. For each cell type, the mean sensitivities $\bar{S}_{\mathcal{Z},T}$ were calculated. Our results indicate that, for the impedance phase, a BMS must measure a change of phase of −0.35° and −0.17° for the low and high temperature ranges, respectively, to detect a temperature change of 1 K. Similarly, when using the imaginary part of the impedance for internal cell temperature estimation, an uncertainty smaller than 41 μΩ is necessary. The required accuracy increases with increasing cell capacity, as the cell impedance decreases with greater capacity. For instance, when using the absolute value of the impedance as $\mathcal{Z}$ for prismatic cells, an uncertainty less than 9 μΩ is needed in the high-temperature range to detect a temperature change of 1 K.

By dividing the sensitivity $S_{\mathcal{Z},T}$ by the value of the impedance feature at 23 °C, we derive the normalized sensitivity $S_{\mathcal{Z},T\,n}$ in $\%\,K^{-1}$, as defined in Eq. (2). This allows for comparison of the normalized temperature sensitivities of different impedance features, as listed in Table 4. The impedance phase and the imaginary part of the impedance show the largest mean normalized sensitivities in the high temperature range, with $-2.1\,\%\,K^{-1}$ and; $-3.1\,\%\,K^{-1}$, respectively. However, $\mathrm{Im}(Z)$ has not been used to estimate the internal cell temperature of large-capacity prismatic cells, in contrast to $\arg(Z)$, which has been utilized for 4 cells. Additionally, 58% of the reviewed studies employ $\arg(Z)$ for T_{int} estimation. Assuming that all authors identified the optimal impedance feature, this strongly suggest the use of the impedance phase for internal cell temperature estimation.

The mean normalized sensitivities of all 86 estimators and impedance features are $-5.1\,\%\,K^{-1}$ and $-1.9\,\%\,K^{-1}$ for temperatures below and above 23 °C, respectively. These values, alongside the specific impedance feature sensitivities, can be used to estimate the required BMS accuracy for detecting a desired temperature change. Simply multiply the mean normalized sensitivity by the measured value of the selected impedance feature at 23 °C at the selected frequency.

Outliers can occur when the value of the impedance feature at 23 °C approaches zero, particularly for the impedance phase. Therefore, we included only normalized sensitivities smaller than $\pm 15\,\%\,K^{-1}$ for calculating the mean normalized sensitivity summarized in Table 4.

The temperature sensitivity of electrochemical processes is independent of the cell's capacity. Thus, we anticipate a constant $S_{\mathcal{Z},T\,n}$ across all cell capacities when measuring identical impedance features

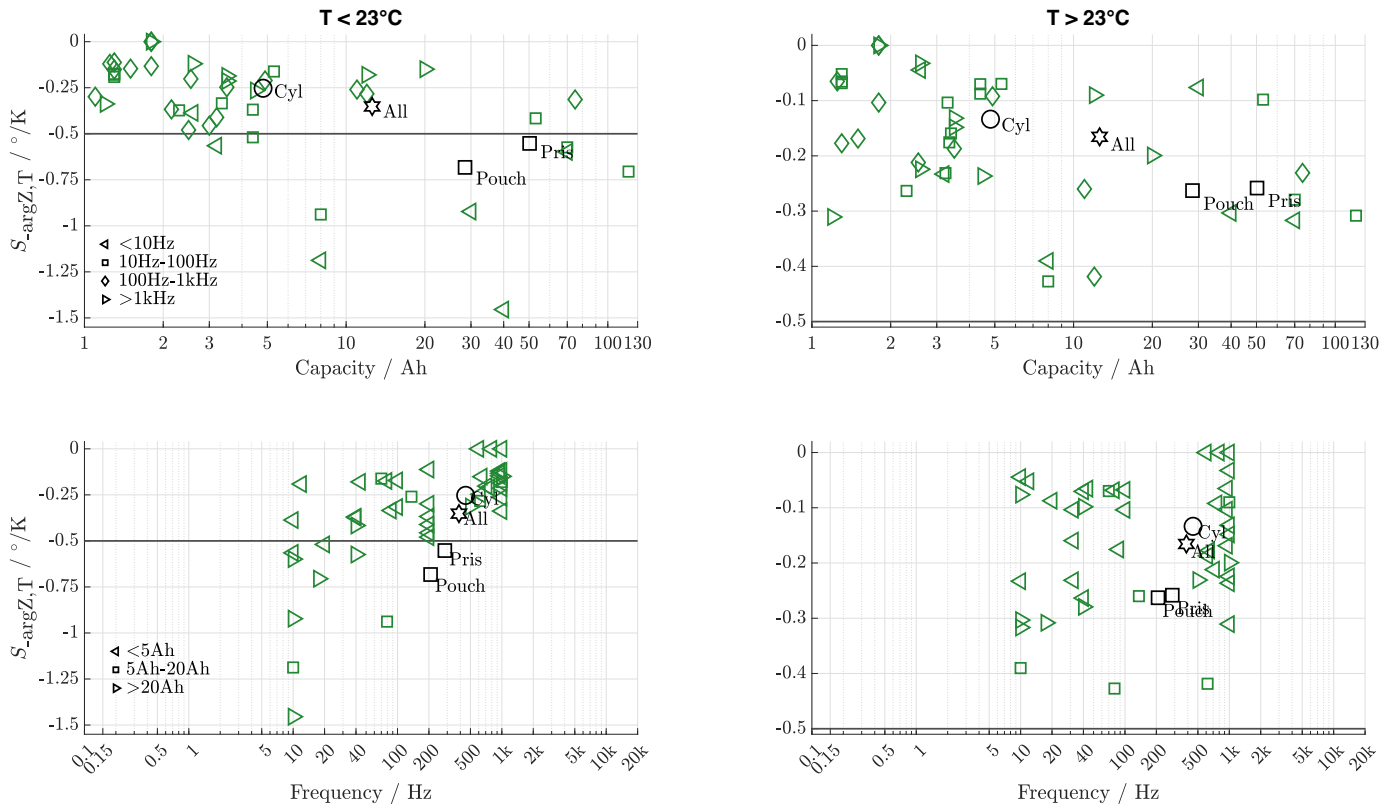

Fig. 4. Impedance phase sensitivities regarding temperature $S_{-\arg(Z),T}$ of the cells listed in Table A.1 (Dataset A) as a function of cell capacity Q and measurement frequency f. The left column depicts the sensitivities for temperatures below 23 °C, and the right column for temperatures above 23 °C. $S_{-\arg(Z),T}$ increases with increasing cell capacity. Conversely, $S_{-\arg(Z),T}$ decreases with increasing temperature and measurement frequency. Black markers indicate mean values.

at frequencies corresponding to equivalent electrochemical processes. However, empirical observations reveal deviations from this expected behavior due to non-uniform impedance scaling with capacity. This non-uniform scaling stems primarily from the transition in cell form factor from cylindrical to prismatic as capacity increases. Figure S15 in Section S2 of the supplementary material depicts this behavior by plotting the absolute value of the impedance at the intercept frequency, representing the ohmic resistance, as a function of cell capacity. The log–log plot exhibits an S-shaped behavior that cannot be adequately fitted with standard functions such as rational or logistic models. Consequently, $S_{\mathcal{Z},T\,n}$ may be larger for cells with higher capacity.

The observed impedance scaling behavior originates from fundamental differences in current collector architectures between cell form factors. Cylindrical cells employ rolled electrode configurations where current collection occurs through centralized terminal connections at opposite ends of the cell [55–58]. In contrast, prismatic cells utilize stacked electrode assemblies with distributed tab arrangements positioned along the cell edges [59,60].

Based on our meta–analysis and measurement results, we suggest the impedance phase as an optimal impedance feature for EIS–based internal cell temperature estimation, regardless of the cell's capacity and chemistry.

4.2. Dataset B: Determining optimal measurement frequency

In Fig. 5, we expanded our analysis to include the entire Dataset B, plotting the five Nyquist features defined in Section 2.2 against cell capacity. A clear trend emerges for the intercept frequency f_{int}, which decreases with increasing capacity. The volumetric energy density, expressed in $\mathrm{W\,h\,L^{-1}}$, is primarily constrained by the thickness of the negative electrode coating [61,62]. Large-format (high-capacity) cells require larger physical dimensions and volumes compared to cells with low capacity. This geometric scaling introduces two effects that reduce the intercept frequency. First, increased cell dimensions result in higher cell inductance as currents flow through larger loop areas, (e.g. longer distance between positive and negative terminal). For additional details on geometric factors affecting cell inductance in cylindrical cells, see Landinger et al. [63]. Second, the larger electrode surface area results in a lower overall impedance.

In contrast, the characteristic arc frequency f_{arc} and the transition frequency f_{t} show a more complex relationship with cell capacity, characterized by a bathtub-like trend. Both frequency ratios, $\alpha_{\text{arc/t}}$ and $\alpha_{\text{int/arc}}$, exhibit a downward trend as cell capacity increases, suggesting that the semicircle spans a narrower frequency range with increased cell capacity. We explain this behavior again with the larger inductive component of cells with higher capacity due to higher volume.

The mean values and Interquartile Ranges (IQRs) of the Nyquist features are summarized in Table 5. The SEI layer significantly influences the high–frequency region of the semicircle, which lies between the intercept frequency f_{int} and the characteristic arc frequency f_{arc} [11,19,34,64,65]. This influence is observed within a frequency range from 100 Hz to 900 Hz for cylindrical cells and from 40 Hz to 400 Hz for prismatic cells. These frequency ranges are optimal for estimating the internal temperature of cells based on the impedance phase and the imaginary component of the impedance.

The physical interpretation of the presented results is left for the scientific community; we limit our scope to an empirical analysis. For analyzing the dependencies of these Nyquist frequency features on SoC, SoH, and temperature of custom 50 mAh pouch cells, we refer to the work of Westerhoff et al. [66]. They concluded that both the intercept and the transition frequency decrease with increased SoC, SoH, and temperature.

In summary, based on our meta–analysis, we recommend using the impedance phase, evaluated at frequencies above 100 Hz and below

Table 3
Mean sensitivities of the impedance features regarding temperature, denoted as $\bar{S}_{\mathcal{Z},\mathrm{T}}$, for temperature ranges $T_1 < 23\,°\mathrm{C}$ and $T_2 > 23\,°\mathrm{C}$, calculated for the cells listed in Table A.1 (Dataset A). This data is categorized by cell form factor (cylindrical, pouch, prismatic) and impedance feature $\mathcal{Z}$. The number of cells (No.) and the ratio of $\bar{S}_{\mathcal{Z},\mathrm{T}_1}$ and $\bar{S}_{\mathcal{Z},\mathrm{T}_2}$ ($R_{S_{\mathcal{Z},\mathrm{T}}}$) are provided. When using the negative impedance phase ($-\arg(Z)$), a Battery Management System (BMS) must resolve a phase change of −0.35° and −0.17° for the low and high temperature ranges, respectively, to detect a temperature change of 1 K. The $R_{S_{\mathcal{Z},\mathrm{T}}}$ values are greater than one for all impedance features, indicating reduced sensitivity at elevated temperatures.

$\mathcal{Z}$	Cylindrical				Pouch				Prismatic			
	No.	$\bar{S}_{\mathcal{Z},\mathrm{T}_1}$	$\bar{S}_{\mathcal{Z},\mathrm{T}_2}$	$R_{S_{\mathcal{Z},\mathrm{T}}}$	No.	$\bar{S}_{\mathcal{Z},\mathrm{T}_1}$	$\bar{S}_{\mathcal{Z},\mathrm{T}_2}$	$R_{S_{\mathcal{Z},\mathrm{T}}}$	No.	$\bar{S}_{\mathcal{Z},\mathrm{T}_1}$	$\bar{S}_{\mathcal{Z},\mathrm{T}_2}$	$R_{S_{\mathcal{Z},\mathrm{T}}}$	No.	$\bar{S}_{\mathcal{Z},\mathrm{T}_1}$	$\bar{S}_{\mathcal{Z},\mathrm{T}_2}$	$R_{S_{\mathcal{Z},\mathrm{T}}}$
		$\mu\Omega\,\mathrm{K}^{-1}$				$\mu\Omega\,\mathrm{K}^{-1}$				$\mu\Omega\,\mathrm{K}^{-1}$				$\mu\Omega\,\mathrm{K}^{-1}$		
$\mathrm{Re}(Z)$	8	−355	−30	11.9	5	−509	−28	18.1	2	−67	−45	1.5	1	−28	−5	5.6
		$\mu\Omega\,\mathrm{K}^{-1}$				$\mu\Omega\,\mathrm{K}^{-1}$				$\mu\Omega\,\mathrm{K}^{-1}$				$\mu\Omega\,\mathrm{K}^{-1}$		
$-\mathrm{Im}(Z)$	12	−140	−41	3.4	10	−133	−33	4.1	1	−122	−59	2.1	0	–	–	–
		$\mu\Omega\,\mathrm{K}^{-1}$				$\mu\Omega\,\mathrm{K}^{-1}$				$\mu\Omega\,\mathrm{K}^{-1}$				$\mu\Omega\,\mathrm{K}^{-1}$		
$\mathrm{abs}(Z)$	11	−209	−28	7.6	4	−512	−50	10.3	2	−126	−31	4.1	5	−23	−9	2.6
		$°\,\mathrm{K}^{-1}$				$°\,\mathrm{K}^{-1}$				$°\,\mathrm{K}^{-1}$				$°\,\mathrm{K}^{-1}$		
$-\arg(Z)$	50	−0.35	−0.17	2.1	34	−0.25	−0.13	1.9	9	−0.68	−0.26	2.6	4	−0.55	−0.26	2.1
		$\mathrm{Hz\,K}^{-1}$				$\mathrm{Hz\,K}^{-1}$				$\mathrm{Hz\,K}^{-1}$				$\mathrm{Hz\,K}^{-1}$		
f_{int}	5	−57	−20	2.8	2	−62	−22	2.9	2	−77	−27	2.9	1	−6	−4	1.4

Table 4
Mean normalized sensitivities of the impedance features regarding temperature, denoted as $\bar{S}_{\mathcal{Z},\mathrm{T\,n}}$, for temperature ranges $T_1 < 23\,°\mathrm{C}$ and $T_2 > 23\,°\mathrm{C}$, calculated for the cells listed in Table A.1 (Dataset A). This data is categorized by cell form factor (cylindrical, pouch, prismatic) and impedance feature $\mathcal{Z}$. The number of cells (No.) and the ratio of $\bar{S}_{\mathcal{Z},\mathrm{T}_1\,\mathrm{n}}$ and $\bar{S}_{\mathcal{Z},\mathrm{T}_2\,\mathrm{n}}$ ($R_{S_{\mathcal{Z},\mathrm{T\,n}}}$) are provided. The mean normalized sensitivity across all 86 estimators and impedance features yields $-5.1\,\%\,\mathrm{K}^{-1}$ and $-1.9\,\%\,\mathrm{K}^{-1}$ for temperatures below and above 23 °C, respectively. The impedance phase and the imaginary part of the impedance exhibit the highest mean normalized sensitivities in the elevated temperature range, specifically $-2.1\,\%\,\mathrm{K}^{-1}$ and $-3.1\,\%\,\mathrm{K}^{-1}$.

$\mathcal{Z}$	Cylindrical				Pouch				Prismatic			
	No.	$\bar{S}_{\mathcal{Z},\mathrm{T}_1\,\mathrm{n}}$ $\%\,\mathrm{K}^{-1}$	$\bar{S}_{\mathcal{Z},\mathrm{T}_2\,\mathrm{n}}$ $\%\,\mathrm{K}^{-1}$	$R_{S_{\mathcal{Z},\mathrm{T\,n}}}$	No.	$\bar{S}_{\mathcal{Z},\mathrm{T}_1\,\mathrm{n}}$ $\%\,\mathrm{K}^{-1}$	$\bar{S}_{\mathcal{Z},\mathrm{T}_2\,\mathrm{n}}$ $\%\,\mathrm{K}^{-1}$	$R_{S_{\mathcal{Z},\mathrm{T\,n}}}$	No.	$\bar{S}_{\mathcal{Z},\mathrm{T}_1\,\mathrm{n}}$ $\%\,\mathrm{K}^{-1}$	$\bar{S}_{\mathcal{Z},\mathrm{T}_2\,\mathrm{n}}$ $\%\,\mathrm{K}^{-1}$	$R_{S_{\mathcal{Z},\mathrm{T\,n}}}$	No.	$\bar{S}_{\mathcal{Z},\mathrm{T}_1\,\mathrm{n}}$ $\%\,\mathrm{K}^{-1}$	$\bar{S}_{\mathcal{Z},\mathrm{T}_2\,\mathrm{n}}$ $\%\,\mathrm{K}^{-1}$	$R_{S_{\mathcal{Z},\mathrm{T\,n}}}$
$\mathrm{Re}(Z)$	8	–2.7	–0.8	3.4	5	–2.7	–0.7	3.8	2	–1.6	–1	1.6	1	–3.5	–0.6	5.6
$-\mathrm{Im}(Z)$	12	–7	–3.1	2.3	10	–7.5	–3.3	2.3	1	–5.3	–2.5	2.1	0	–	–	–
$\mathrm{abs}(Z)$	11	–3.3	–0.8	3.9	4	–0.9	–0.3	3.2	2	–6.6	–1.6	4.1	5	–2.9	–0.9	3.3
$-\arg(Z)$	50	–5.3	–2.1	2.5	34	–4.2	–1.6	2.7	9	–7.4	–1.6	2.2	4	–7.8	–3.1	2.5
f_{int}	5	–4.7	–1.7	2.7	2	–5.5	–2	2.8	2	–6.1	–2.3	2.7	1	–0.3	–0.3	1.4
All	86	–5.1	–1.9	2.7	55	–4.6	–1.7	2.7	16	–6.4	–2.6	2.5	11	–4.7	–1.6	2.9

1 kHz, to estimate internal cell temperature. Our findings indicate average temperature sensitivities of $-0.35\,°\,\mathrm{K}^{-1}$ for temperatures below 23 °C and $-0.17\,°\,\mathrm{K}^{-1}$ for temperatures above 23 °C. Importantly, the sensitivities remain constant, regardless of the cell's capacity and chemistry. However, we emphasize that data points for capacities exceeding 20 Ah are limited, which may compromise the accuracy and reliability of the observed trends within this range.

4.3. Establishing accuracy requirements for EIS–enabled BMS in internal cell temperature estimation

In this section, we derive the accuracy requirements for BMSs equipped with EIS capability, specifically for the online estimation of internal cell temperatures. We also evaluate the performance of existing BMS hardware based on previously calculated sensitivities.

Single-cell supervisor integrated circuits capable of measuring the impedance of individual cells within a stack were used as BMS [67,68]. Beelen et al. [68] reported a standard deviation, denoted as σ, for the real and imaginary parts of the impedance, ranging from 10 μΩ to 15 μΩ across a frequency range of 0.1 kHz to 1 kHz when measured on a 23 Ah cell. Strasser et al. [67] used a different single–cell supervisor integrated circuit and measured a 60 Ah prismatic cell, reporting a standard deviation in the range of 1.3 μΩ to 5 μΩ for the same frequency range.

An integrated circuit featuring 14 channels and EIS capabilities from 100 mHz to 5 kHz was introduced by Ito et al. [69]. Comparative measurements of seven stacked 3.4 Ah cells against laboratory measurement equipment achieved a phase error of less than 1° across the entire frequency range; however, no uncertainties were reported. Similarly, Zhang et al. [70] presented results from a commercially available BMS integrated circuit for four stacked 2.9 Ah cells, demonstrating a phase difference of less than 1° from 100 mHz to 1.16 kHz compared to laboratory measurements, again without reporting measurement uncertainties.

By using the aforementioned uncertainties for the real and imaginary parts of the impedance, we apply the propagation of uncertainty principle to calculate the standard deviation of the impedance phase, denoted as $\sigma_{\arg(Z)}$:

$$\sigma_{\arg(Z)} = \sqrt{\left(\frac{\partial \arg(Z)}{\partial \mathrm{Re}(Z)}\right)^2 \sigma^2_{\mathrm{Re}(Z)} + \left(\frac{\partial \arg(Z)}{\partial \mathrm{Im}(Z)}\right)^2 \sigma^2_{\mathrm{Im}(Z)}} \tag{3}$$

$$= \sqrt{\left(-\frac{\mathrm{Im}(Z)}{\mathrm{Re}(Z)^2 + \mathrm{Im}(Z)^2}\right)^2 \sigma^2_{\mathrm{Re}(Z)} + \left(\frac{\mathrm{Re}(Z)}{\mathrm{Re}(Z)^2 + \mathrm{Im}(Z)^2}\right)^2 \sigma^2_{\mathrm{Im}(Z)}}\,. \tag{4}$$

Subsequently, we estimate the uncertainty associated with EIS–based internal cell temperature estimation, $\sigma_{T_{\mathrm{int}}}$, by calculating the phase uncertainty and dividing it by the previously derived mean sensitivities $\bar{S}_{\arg(Z),\mathrm{T}}$:

$$\sigma_{T_{\mathrm{int}}} = \frac{\sigma_{\arg(Z)}}{\bar{S}_{\arg(Z),\mathrm{T}}}\,. \tag{5}$$

To determine $\sigma_{\arg(Z)}$, we used the mean values for the real and imaginary parts of the impedance measured at the characteristic arc

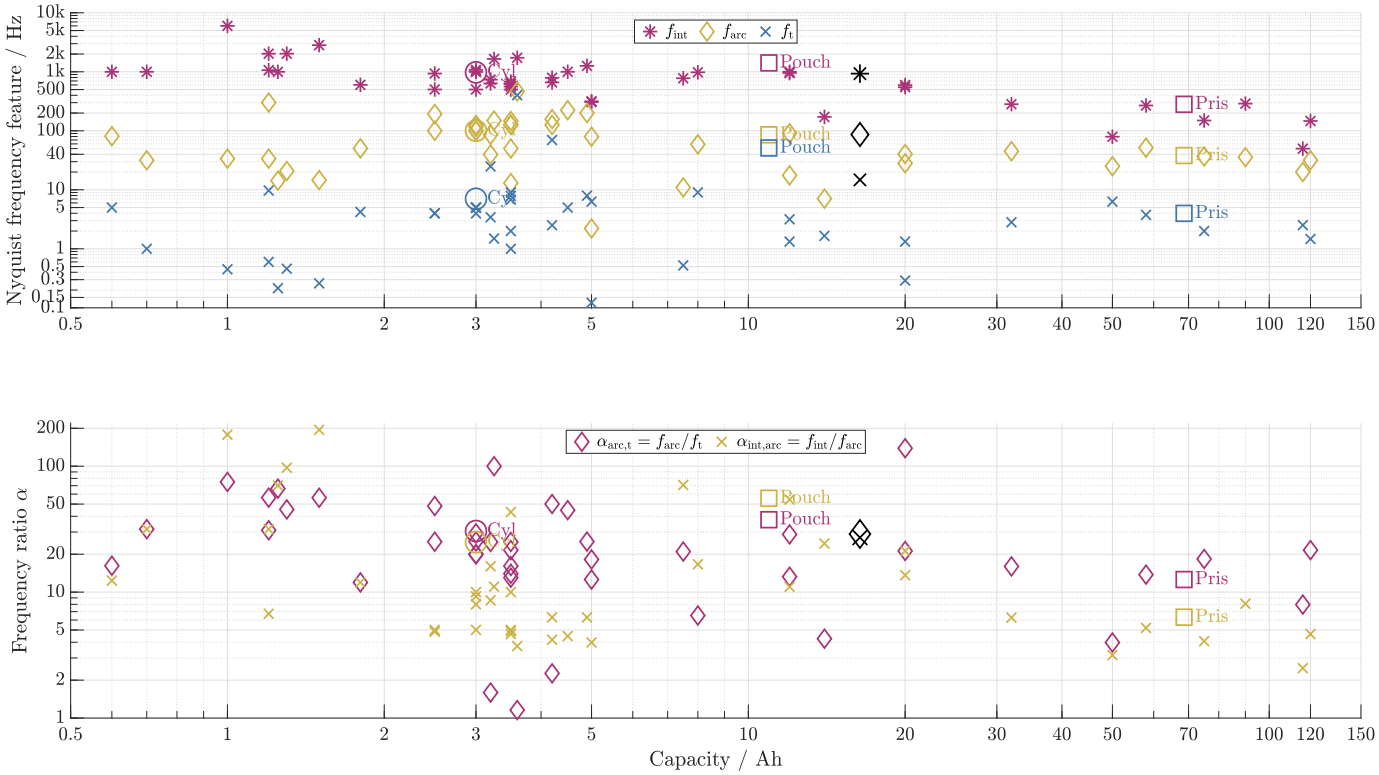

Fig. 5. Nyquist curve frequency features extracted from the Electrochemical Impedance Spectroscopy (EIS) data listed in Table B.1 (Dataset B) as a function of cell capacity. The intercept frequency f_{int} decreases with increasing capacity. No clear trend is determined for the characteristic arc frequency f_{arc} and the transition frequency f_t. Both frequency ratios, $\alpha_{arc/t} = f_{arc}/f_t$ and $\alpha_{int/arc} = f_{int}/f_{arc}$, decrease with increasing capacity, indicating that the semicircle spans a narrower frequency range as cell capacity increases. Larger markers indicate mean values. The Nyquist curve features are defined in Fig. 3.

frequency from Dataset B for cylindrical, pouch, and prismatic cells. The summarized results, including σ_{arg} and $\sigma_{T_{int}}$, are presented in Table 6. The calculated uncertainties for high–capacity prismatic cells at temperatures above 23 °C are 2.4 K and 0.4 K, corresponding to standard deviations of 10 μΩ and 1.5 μΩ for the real and imaginary components, respectively.

For obtaining a temperature uncertainty $\sigma_{T_{int}}$ of 1 K, the measurement system must achieve an uncertainty smaller than 4 μΩ for both the real and imaginary parts of the impedance. To ensure that all estimated values fall within ±1 K with a probability of 99.7%, the requirement is $\sigma_{Re(Z),Im(Z)}$ smaller than 1.3 μΩ.

5. Results and discussion – Impact of battery–powered traction application noise on online EIS

Battery–powered traction applications convert electrical energy into mechanical energy for propulsion, e.g. EVs. A critical component of this systems is the traction inverter, which converts the dc battery voltage into an ac control signal, generating the rotating magnetic field int the electric motor. In EVs, traction inverters operate at switching frequencies ranging from 5 kHz to 20 kHz [71]. The frequency of the electric motor control signal, denoted as f_{el}, depends on the velocity of the EV. As the velocity increases, the motor's mechanical rotational frequency, f_{rot}, also increases, requiring a higher f_{el}. The relationship is governed by the motor's pole pair configuration and can be expressed mathematically as:

$$f_{el} = f_{rot} \cdot N_P\,, \tag{6}$$

where N_P represents the number of pole pairs.

Using the equation presented above, along with data from EVs compiled in Table C.1, we anticipate that the maximum fundamental frequency component for electric motor control, denoted as $f_{el,max}$, will remain below 1.4 kHz. Our analysis includes a diverse selection of 60 EVs, representing both low-end and high-end EVs. The distribution of $f_{el,max}$ is illustrated in Fig. 6. It is important to note that this value reflects only the fundamental frequency component.

The actual drivetrain noise spectrum is more complex due to Pulse–Width Modulation (PWM) switching schemes. These motor control strategies generate harmonics of the fundamental frequency and intermodulation products between f_{el} and the PWM switching frequency [72,73]. The resulting noise characteristics vary considerably depending on the specific PWM algorithms and motor control strategies implemented, which differ across vehicle manufacturers and traction applications.

In the preceding section, we identified an optimal frequency range of 100 Hz to 1 kHz for internal cell temperature estimation based on impedance phase measurements. Our suggested measurement frequency range overlaps with the noise frequencies inherent in traction applications, specifically in EVs. This interference can potentially introduce errors in the impedance measurements and consequently affect estimates of internal cell temperature.

However, the value of the frequency of the electric motor control signal f_{el} is variable, dependent on the EV's speed, which in turn is influenced by the driver's style, infrastructure, traffic conditions, and weather. While interference may not be present at all times, it is essential to acknowledge that individual measurements can be disrupted. It is advisable that the measured impedance values be assessed for

Table 5
Mean cell capacities $\bar{Q}$, mean Nyquist curve features and their respective Interquartile Range (IQR) for cylindrical, pouch, and prismatic cells included in Dataset B, as listed in Table B.1. The Solid Electrolyte Interphase (SEI) layer dominates in a frequency range from 100 Hz to 900 Hz for cylindrical cells and from 40 Hz to 400 Hz for prismatic cells. The frequency ratios $\bar{\alpha}_{\mathrm{int/arc}} = \bar{f}_{\mathrm{int}}/\bar{f}_{\mathrm{arc}}$ and $\bar{\alpha}_{\mathrm{arc/t}} = \bar{f}_{\mathrm{arc}}/\bar{f}_{\mathrm{t}}$ decrease with increasing cell capacity, indicating a smaller frequency range spanned by the semicircle as cell capacity rises. The number of cells (No.) is also reported. A more detailed statistical analysis is included in Section S2 of the supplementary material linked in Appendix D.

		Cylindrical	Pouch	Prismatic
No.		28	8	8
$\bar{Q}$	Ah	3	11	68.6
Q_{IQR}	Ah	1.9	12.7	62
$\bar{f}_{\mathrm{int}}$	kHz	0.98	1.41	0.28
$f_{\mathrm{int,IQR}}$	Hz	410	938	173
$\bar{f}_{\mathrm{arc}}$	Hz	101	85	38
$f_{\mathrm{arc,IQR}}$	Hz	100	53	20
$\bar{f}_{\mathrm{t}}$	Hz	7	51	4
$f_{\mathrm{t,IQR}}$	Hz	5.3	2	3.5
$\bar{\alpha}_{\mathrm{int/arc}}$		25	56	6
$\alpha_{\mathrm{int/arc,IQR}}$		19	84	3.6
$\bar{\alpha}_{\mathrm{arc/t}}$		31	38	13
$\alpha_{\mathrm{arc/t,IQR}}$		29	43	11

Table 6
Uncertainties in internal cell temperature estimation for temperatures above 23 °C, calculated from impedance phase data. Standard deviations of 1.5 μΩ and 10 μΩ [67,68] for the real and imaginary parts of impedance were used to calculate the standard deviation of the impedance phase $\sigma_{\arg(Z)}$. The mean real and imaginary values of the impedance measured at the charge transfer frequency f_{arc}, denoted as $\overline{\mathrm{Re}}(Z(f_{\mathrm{arc}}))$ and $\overline{\mathrm{Im}}(Z(f_{\mathrm{arc}}))$, obtained from Dataset B (Table B.1), were used for this calculation. The standard deviation of the internal cell temperature $\sigma_{T_{\mathrm{int}}}$ was derived with the mean sensitivities $\bar{S}_{\arg(Z),\mathrm{T_2}}$ from Dataset A (Table A.1) using Eq. (5). The calculated uncertainties for high–energy prismatic cells at temperatures exceeding 23 °C are 2.4 K and 0.4 K, corresponding to standard deviations of 10 μΩ and 1.5 μΩ for both the real and imaginary components.

		Cylindrical	Pouch	Prismatic
$\overline{\mathrm{Re}}\left(Z(f_{\mathrm{arc}})\right)$	mΩ	26.5	11	0.96
$\overline{\mathrm{Im}}\left(Z(f_{\mathrm{arc}})\right)$	mΩ	−4.1	−2.4	−0.15
$\bar{S}_{\arg(Z),\mathrm{T_2}}$	$^\circ\,\mathrm{K}^{-1}$	−0.13	−0.26	−0.26
		$\sigma_{\mathbf{Re}(Z),\mathbf{Im}(Z)} = 10\,\mu\Omega$		
$\sigma_{\arg(Z)}$	°	0.02	0.05	0.6
$\sigma_{T_{\mathrm{int}}}$	K	0.18	0.18	2.4
		$\sigma_{\mathbf{Re}(Z),\mathbf{Im}(Z)} = 1.5\,\mu\Omega$		
$\sigma_{\arg(Z)}$	°	0.002	0.007	0.09
$\sigma_{T_{\mathrm{int}}}$	K	0.03	0.03	0.36

plausibility, and employing a range of measurement frequencies may help mitigate interference.

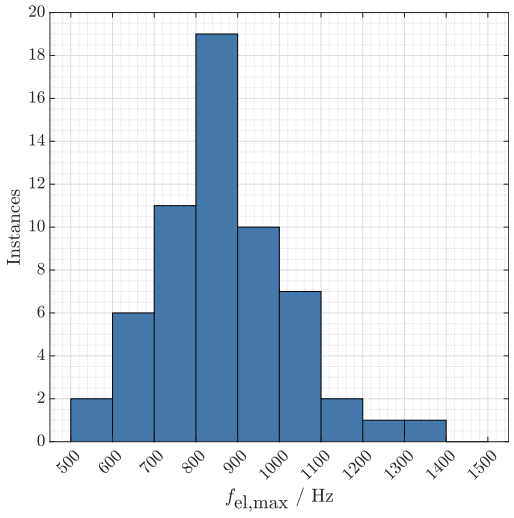

Fig. 6. Histogram of the maximum motor control signal frequency $f_{\mathrm{el,max}}$ as listed in Table C.1. For the 60 selected Electric Vehicles (EVs), spanning both low–end and high–end categories, $f_{\mathrm{el,max}}$ ranges from 500 Hz to 1.4 kHz.

5.1. Real–world EV traction noise

Raijmakers et al. measured the battery pack current of an EV during acceleration and regenerative breaking on a test bench [30]. They observed that the magnitude of the spectral components of the current peaked at approximately 200 Hz and decreased with increasing frequency.

In a similar experiment, we measured the battery pack current of a Citroën C-Zero, following the methodology detailed in Section 3.2. The battery pack current during a 1.7 min dynamic drive, sampled at 50 kHz, is shown at the top Fig. 7. Positive currents indicate battery discharge (acceleration), while negative currents represent battery charge (recuperation). Discharge currents reached up to 3.8 C, and recuperation currents peaked at 1.6 C. The spectral components of the current for each time step were estimated using STFT. The resulting spectrogram, depicted at the bottom of Fig. 7, is expressed as a Power Spectral Density (PSD) in $\mathrm{dB\,Hz^{-1}}$. A Hann window of length 2 kS, with an Equivalent Noise Bandwidth (ENBW) of 30 Hz and a 75% overlap, was employed.

Throughout the test drive, the PWM switching of the traction inverter, around 7 kHz, was observed. The frequency f_{el} of the electrical motor control and its harmonics were evident below 3 kHz. During acceleration, both the frequency and magnitude of this control signal increased as the electric motor's speed increased. Conversely, during deceleration, both parameters decreased, as observed from 25 s to 35 s and 62 s to 72 s. At peak currents, the maximum f_{el} reached 1.3 kHz.

To validate our experimental observations against theoretical predictions, the vehicle-specific parameters for the Citroën C-Zero listed in Table C.1 were substituted into the traction motor frequency relationship given by Eq. (6):

$$f_{\mathrm{el,max}} = \frac{8800\,\mathrm{rpm}}{60} \cdot 4 = 587\,\mathrm{Hz}\,. \tag{7}$$

The observed discrepancy, where experimental measurements are approximately 2.2 times higher than the theoretical maximum f_{el}, can be attributed to the specific PWM switching scheme implemented in the motor control unit. The equation above accounts only for the fundamental frequency component required for motor control. However, additional frequency components, including higher-order harmonics of the fundamental frequency and intermodulation products, are generated by the motor control algorithm.

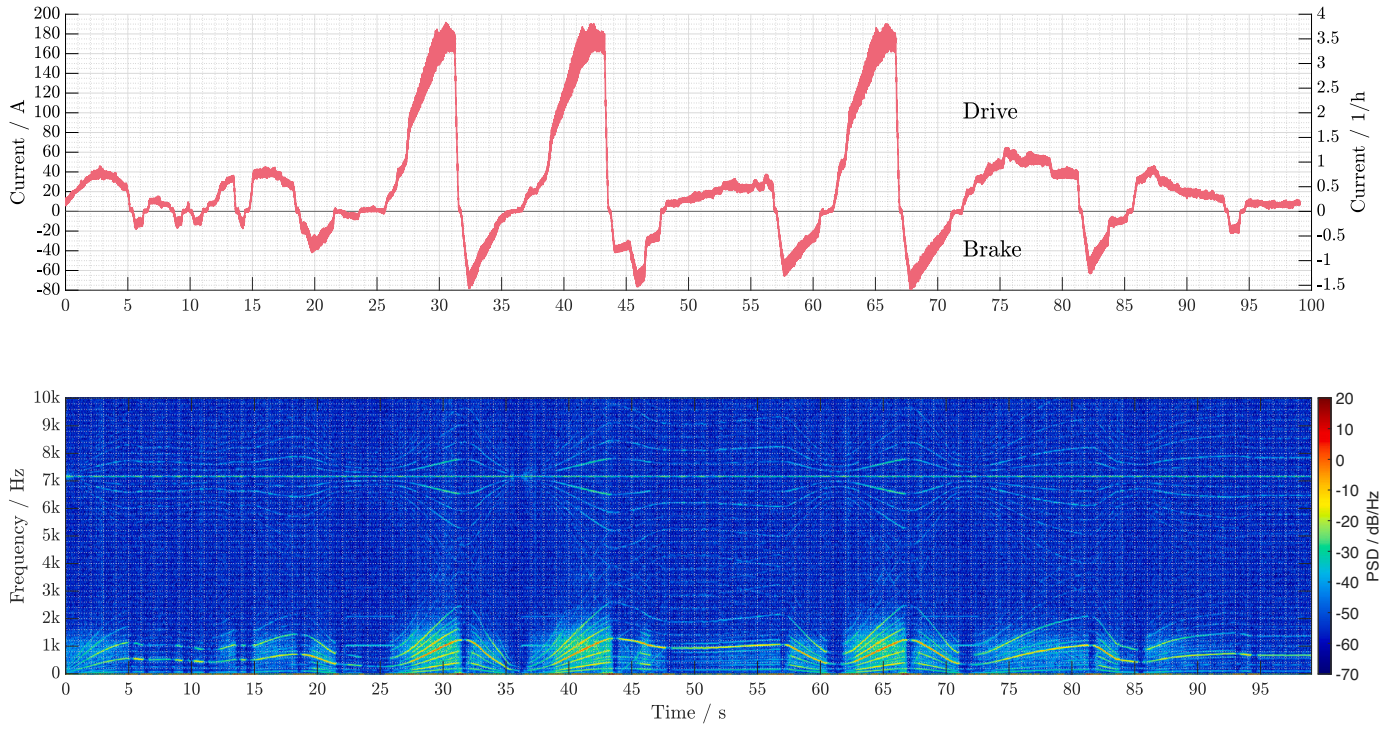

Fig. 7. Battery pack current of a Citroën C-Zero measured with a Hioki 3275 current clamp [51] and a PicoScope 5444D oscilloscope [52] at the traction inverter input during a dynamic test drive. **Top**: The waveform of the battery pack current in the time domain, sampled at 50 kHz. Positive currents indicate battery discharge (acceleration), while negative currents represent battery charging (recuperation). **Bottom**: The Short–Time Fourier transform (STFT) of the battery pack current, scaled to a Power Spectral Density (PSD). A Hann window of length 2 kS with an Equivalent Noise Bandwidth (ENBW) of 30 Hz and a 75% overlap was applied. The traction inverter's Pulse–Width Modulation (PWM) switching frequency, approximately 7 kHz, is present throughout the entire test drive. The frequency f_{el} of the electrical motor control signal generated by the traction inverter and its harmonics are visible below 3 kHz. During acceleration, both frequency and magnitude of this control signal increase as the electric motor speed rises, whereas during deceleration, the frequency decreases.

To quantify the traction inverter's noise, we estimated the PSD using Welch's method across all driving scenarios. For this analysis, a flat top window with an ENBW of 18.9 Hz and a 50% overlap was used. From each individual PSD, the maximum PSD value within each frequency bin, ranging from 5 Hz to 25 kHz, was calculated. This analysis yields a noise envelope for the traction inverter's PSD, quantifying the frequency components and power of the interference. The results, based on the Citroën C-Zero, are shown in Fig. 8. High noise power occurs at frequencies below 100 Hz, whereas the control signal of the traction inverter extends up to 1 kHz. At 1 kHz, the PSD estimates $-15\,\mathrm{dB\,Hz^{-1}}$, corresponding to a current amplitude of approximately 0.8 A. This relationship can be expressed mathematically as follows:

$$\sqrt{\left(10^{\mathrm{PSD}/10}\right)\cdot \mathrm{ENBW}}\,. \tag{8}$$

At 7 kHz, 14 kHz, and 21 kHz the traction inverter's PWM switching frequency and its harmonics dominate. These findings are consistent with those presented by Raijmakers et al. [30] and our traction inverter noise model.

On the one hand, the traction inverter noise may interfere with online EIS measurements that use active excitation, as noise components overlap with the optimal measurement frequency range for internal cell temperature estimation; on the other hand, this noise could be used as excitation for EIS itself as proposed by previous studies [107–111], referred to as passive EIS.

In conclusion, traction inverters generate significant noise power that can interfere with online EIS measurements. We identified two noise sources with different characteristics.

Below 3 kHz, the electric motor control signal, its harmonics, and intermodulation products, dominate the noise spectrum. Peak noise power is concentrated below 100 Hz, where signal–to–noise ratios are insufficient for reliable measurements; consequently, EIS measurements should avoid this frequency range. Noise levels decrease substantially above 1.3 kHz; however, impedance sensitivity regarding temperature also typically decreases with increasing frequency, limiting the accuracy of temperature estimation at higher frequencies. This low–frequency motor control noise correlates with driving behavior and varies dynamically during operation.

The second noise source originates from the inverter switching frequency (5 kHz to 20 kHz) and its harmonics. Although this switching noise exhibits lower power spectral density compared to motor control noise, it persists continuously during inverter operation.

Despite these challenges, online EIS–based temperature estimation remains feasible. We recommend using a range of measurement frequencies and outlier detection for more robust estimates. The optimal approach balances the cell's impedance sensitivity to temperature against the noise profile of the specific traction application.

6. Conclusion

In conclusion, our study highlights practical considerations for online EIS–based battery internal temperature estimation in traction applications. It is essential to account not only for the electrochemical properties of the cells but also for the system characteristics inherent to the application for identifying the optimal impedance feature and measurement frequency for accurate internal temperature estimation.

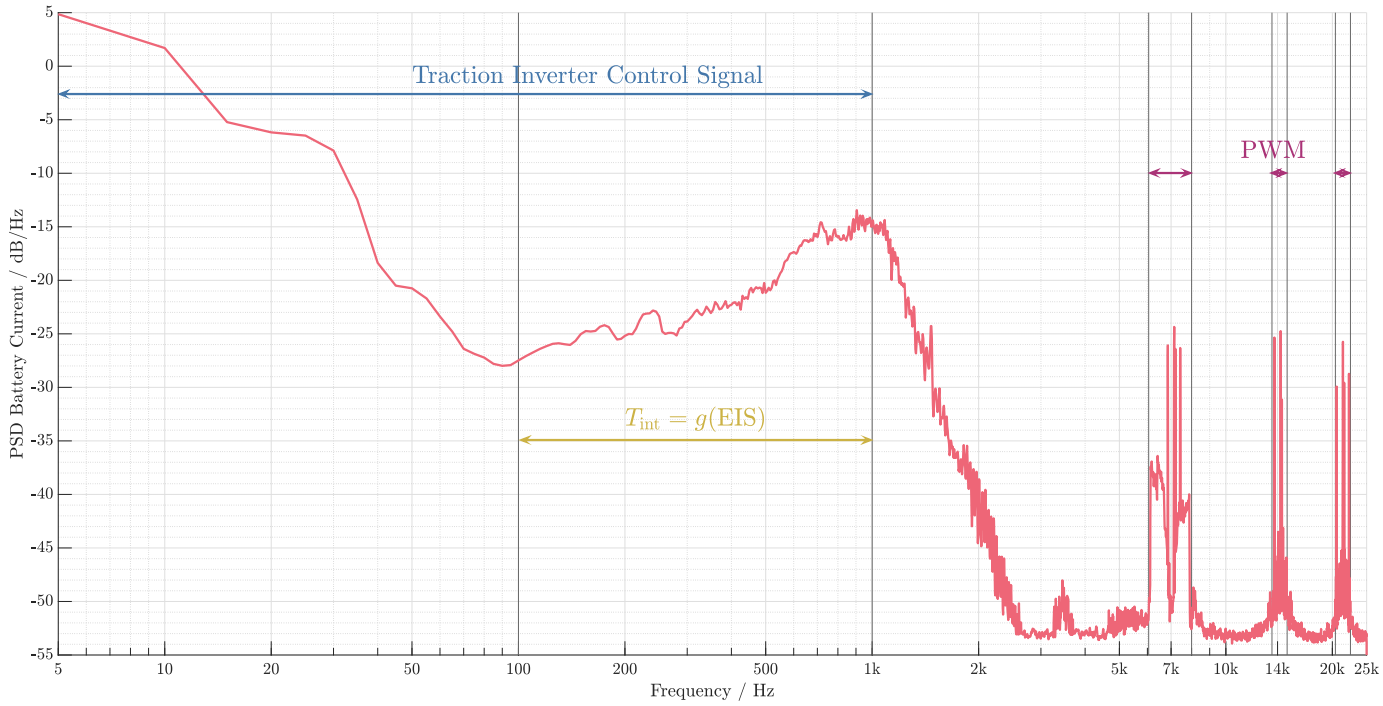

Fig. 8. Power Spectral Density (PSD) envelope of the battery pack current of a Citroën C-Zero measured with a Hioki 3275 current clamp [51] and a PicoScope 5444D oscilloscope [52] at the traction inverter input during various drive modes: parking, acceleration, regenerative braking, constant velocity driving, urban driving, and dynamic driving (refer to Fig. 7). A flat top window with Equivalent Noise Bandwidth (ENBW) of 18.9 Hz and a 50% overlap was applied to estimate the PSD using Welch's method. Oscilloscope sample rates varied between 50 kHz and 20 MHz. The maximum PSD value at each frequency bin across all drive profiles yields the envelope, which quantifies the traction inverter's noise power and its frequency content. The traction inverter's control signal is present up to 1 kHz. At 1 kHz, the PSD estimates $-15\,\text{dB}\,\text{Hz}^{-1}$, corresponds to an amplitude of approximately 0.8 A (refer to Eq. (8)). At frequencies of 7 kHz, 14 kHz, and 21 kHz, the Pulse–Width Modulation (PWM) switching frequency of the traction inverter and its harmonics occur. This traction inverter noise overlaps with the optimal Electrochemical Impedance Spectroscopy (EIS) measurement frequency range (100 Hz to 1 kHz) that we identified for internal cell temperature estimation in Section 4.2.

Through a systematic analysis scheme of two datasets, which include 68 existing studies comprising a total of 83 cells and our own experimental results, we identified the impedance phase, evaluated at frequencies between 100 Hz and 1 kHz, as an optimal estimator for internal cell temperature. Our findings indicate mean temperature sensitivities of $-0.35\,°\,\text{K}^{-1}$ for temperatures above 23 °C and $-0.17\,°\,\text{K}^{-1}$ for temperatures below 23 °C. Notably, these sensitivities remain constant regardless of the cell's capacity and chemistry.

To achieve a temperature uncertainty of less than 1 K for large–format cells operating above 23 °C, an EIS measurement system must maintain an uncertainty less than 4 μΩ for both the real and imaginary components of the impedance, based on the observed mean sensitivities. For small-format cells with higher internal resistances, the measurement uncertainty requirement for impedance can be reduced accordingly.

In traction applications, noise generated by the traction inverters can interfere with online EIS measurements at significant power levels. Two noise sources exist: below 3 kHz, motor control signals generate high-power noise that varies with motor speed, while above 5 kHz, switching frequencies generate lower-power noise that remains continuously present during operation. Both noise sources can disturb individual measurements. Employing a range of measurement frequencies, depending on the noise profile of the specific traction application, and outlier detection can mitigate interference; however, it should be noted that merely using frequencies higher than the noise content may not be practical, as impedance sensitivity to temperature typically decreases with increasing measurement frequency.

These findings underscore the importance of precision in EIS measurements to enhance the performance and reliability of BMS in traction applications.

CRediT authorship contribution statement

Norbert Sailer: Writing – original draft, Visualization, Methodology, Investigation, Data curation, Conceptualization. **Christoph Steffan:** Writing – review & editing, Validation, Supervision. **Jan Philipp Schmidt:** Writing – review & editing, Validation, Supervision.

Declaration of Generative AI and AI-assisted technologies in the writing process

During the preparation of this work, the authors used GPT–4o by OpenAI and Claude Sonnet 4 by Anthropic PBC, in order to improve the readability and language of the manuscript. After using these tools/services, the authors reviewed and edited the content as needed and take full responsibility for the content of the published article.

Acknowledgments

This work has been funded by the European Union under the Horizon Europe programme (Grant Agreement No. 101102944). I would like to express my sincere gratitude to Alexander Thaler and Allan Tengg from Virtual Vehicle Research GmbH for their invaluable support in conducting electric vehicle measurements. Furthermore, I appreciate the insightful discussions with Günter Hofer from Infineon Technologies Austria AG and Mario Auer from Graz University of Technology, which greatly contributed to the depth and quality of this research. I would also like to express my gratitude to Luc Raijmakers for providing previously unpublished data.

Appendix A. Dataset A

See Table A.1.

Appendix B. Dataset B

See Table B.1.

Table A.1
Dataset A: Summary of Electrochemical Impedance Spectroscopy (EIS) based internal cell temperature estimators. The impedance feature $\mathcal{Z}$ is evaluated at frequency f to estimate the internal cell temperature. The impedance features used include absolute impedance $\mathrm{abs}(Z)$, impedance phase $\arg(Z)$, real part of impedance $\mathrm{Re}(Z)$, imaginary part of impedance $\mathrm{Im}(Z)$, and intercept frequency $f_{\mathrm{int}} := \mathrm{Im}(Z(f)) = 0$ [27]. The temperature sensitivities $S_{\mathcal{Z},\mathrm{T}}$ of the impedance features were calculated for temperatures below and above 23 °C by linear interpolation, yielding $S_{\mathcal{Z},\mathrm{T_1}}$ and $S_{\mathcal{Z},\mathrm{T_2}}$, respectively. The normalized sensitivity of the impedance feature regarding temperature $S_{\mathcal{Z},\mathrm{T\,n}}$ in $\%\,\mathrm{K}^{-1}$ is calculated by dividing $S_{\mathcal{Z},\mathrm{T}}$ by the value of the impedance feature at 23 °C. The nominal cell capacity Q is expressed in Ah, and the active materials for both the negative and positive electrode (Neg/Pos) are also provided. Data sources are indicated in the second column, where 'Exp' denotes experimental data, 'Fit' refers to a fitted model, and 'WPD' denotes the use of the WebPlotDigitizer tool [45] for data extraction from graphical plots. Publications are organized in chronological order, with the earliest publication date listed first. Data marked with '?' indicates information that was not reported in the original studies.

Ref.	Data Source	$\mathcal{Z}$	f Hz	$\lvert S_{\mathcal{Z},\mathrm{T_1}}\rvert$		$\lvert S_{\mathcal{Z},\mathrm{T_1\,n}}\rvert$ $\%\,\mathrm{K}^{-1}$	$\lvert S_{\mathcal{Z},\mathrm{T_2}}\rvert$		$\lvert S_{\mathcal{Z},\mathrm{T_2\,n}}\rvert$ $\%\,\mathrm{K}^{-1}$	Q Ah	Neg/Pos
[74]	WPD	$\mathrm{abs}(Z)$	0.1	968	$\mu\Omega\,\mathrm{K}^{-1}$	73.2	41	$\mu\Omega\,\mathrm{K}^{-1}$	3.1	6.5	G/NCA
[19]	WPD	$\arg(Z)$	40	0.42	$^\circ\,\mathrm{K}^{-1}$	11.4	0.1	$^\circ\,\mathrm{K}^{-1}$	2.7	53	G/LCO
				0.37	$^\circ\,\mathrm{K}^{-1}$	10.7	0.07	$^\circ\,\mathrm{K}^{-1}$	2	4.4	G/?
				0.37	$^\circ\,\mathrm{K}^{-1}$	4.2	0.26	$^\circ\,\mathrm{K}^{-1}$	3	2.3	G/LFP
[11]	WPD	$\mathrm{Re}(Z)$	10300	67.4	$\mu\Omega\,\mathrm{K}^{-1}$	1.6	45.7	$\mu\Omega\,\mathrm{K}^{-1}$	1.1	2	G/NCA
[27]	WPD	f_{int}	–[a]	99.3	$\mathrm{Hz\,K}^{-1}$	6.3	32.8	$\mathrm{Hz\,K}^{-1}$	2.1	2.3	G/LFP
			–[b]	25.7	$\mathrm{Hz\,K}^{-1}$	4.7	10.2	$\mathrm{Hz\,K}^{-1}$	1.9	7.5	G/NCA
[75]	Fit	$\arg(Z)$	20	0.5	$^\circ\,\mathrm{K}^{-1}$	12.9	0.09	$^\circ\,\mathrm{K}^{-1}$	2.2	4.4	G/LMO
			100	0.3	$^\circ\,\mathrm{K}^{-1}$	6.4	0.1	$^\circ\,\mathrm{K}^{-1}$	2.1		
[10]	WPD	$\mathrm{Re}(Z)$	215	179	$\mu\Omega\,\mathrm{K}^{-1}$	6.5	71	$\mu\Omega\,\mathrm{K}^{-1}$	2.6	2.3	G/LFP
[26]	WPD	$\mathrm{abs}(Z)$	10	205	$\mu\Omega\,\mathrm{K}^{-1}$	9.8	50	$\mu\Omega\,\mathrm{K}^{-1}$	2.4	8	?/?
		$\arg(Z)$		1.2	$^\circ\,\mathrm{K}^{-1}$	11.1	0.4	$^\circ\,\mathrm{K}^{-1}$	3.6		
[65]	Fit	$\mathrm{Im}(Z)$	300	245	$\mu\Omega\,\mathrm{K}^{-1}$	9.6	105	$\mu\Omega\,\mathrm{K}^{-1}$	4.1	2.6	?/LCO
[76]	Fit	$\arg(Z)$	70	0.16	$^\circ\,\mathrm{K}^{-1}$	4.8	0.07	$^\circ\,\mathrm{K}^{-1}$	2.1	5.3	G/LMO
[77]	WPD	$\arg(Z)$	1000	0.15	$^\circ\,\mathrm{K}^{-1}$	1.2	0.2	$^\circ\,\mathrm{K}^{-1}$	1.6	20	LTO/?
[78]	WPD	$\arg(Z)$	80	0.94	$^\circ\,\mathrm{K}^{-1}$	6.6	0.43	$^\circ\,\mathrm{K}^{-1}$	3	8	?/LFP
[30]	WPD	f_{int}[c]	–[d]	5.9	$\mathrm{Hz\,K}^{-1}$	0.4	4.3	$\mathrm{Hz\,K}^{-1}$	0.3	90	G/LFP
[6]	WPD	$\mathrm{Im}(Z)$	215	33	$\mu\Omega\,\mathrm{K}^{-1}$	8.3	–	–	–	4.4	G/LFP
[79]	WPD	$\arg(Z)$	10	0.92	$^\circ\,\mathrm{K}^{-1}$	26.2	0.08	$^\circ\,\mathrm{K}^{-1}$	2.2	30	G/LFP
[80]	WPD	$\mathrm{abs}(Z)$	500	8	$\mu\Omega\,\mathrm{K}^{-1}$	1.2	4.5	$\mu\Omega\,\mathrm{K}^{-1}$	0.7	26	G/NMC
[81]	WPD	$\mathrm{abs}(Z)$	200	174	$\mu\Omega\,\mathrm{K}^{-1}$	1.1	72	$\mu\Omega\,\mathrm{K}^{-1}$	0.45	2.6	?/LFP
	Fit	$\mathrm{Im}(Z)$		164	$\mu\Omega\,\mathrm{K}^{-1}$	8.1	50	$\mu\Omega\,\mathrm{K}^{-1}$	2.5		
	WPD	$\mathrm{Re}(Z)$		138	$\mu\Omega\,\mathrm{K}^{-1}$	0.9	71	$\mu\Omega\,\mathrm{K}^{-1}$	0.5		
[82]	Fit	f_{int}	–[e]	35	$\mathrm{Hz\,K}^{-1}$	3.8	20.9	$\mathrm{Hz\,K}^{-1}$	2.3	12	?/NCA
		$\arg(Z)$	1000	0.18	$^\circ\,\mathrm{K}^{-1}$	32.7	0.09	$^\circ\,\mathrm{K}^{-1}$	16.4		
[83]	Fit	$\mathrm{Re}(Z)$	8	1.3	$\mathrm{m\Omega\,K}^{-1}$	2.9	–	–	–	8	?/?
[84]	WPD	$\mathrm{abs}(Z)$	300	394	$\mu\Omega\,\mathrm{K}^{-1}$	0.7	32	$\mu\Omega\,\mathrm{K}^{-1}$	0.05	2.6	?/LCO
		$\mathrm{Re}(Z)$		385	$\mu\Omega\,\mathrm{K}^{-1}$	0.7	34	$\mu\Omega\,\mathrm{K}^{-1}$	0.06		
[85]	Fit	$\arg(Z)$	10	1.5	$^\circ\,\mathrm{K}^{-1}$	14	0.3	$^\circ\,\mathrm{K}^{-1}$	2.9	40	?/LFP
[25]	Fit	$\arg(Z)$	12	0.19	$^\circ\,\mathrm{K}^{-1}$	8.7	0.05	$^\circ\,\mathrm{K}^{-1}$	2.4	1.3	?/LFP
			44	0.18	$^\circ\,\mathrm{K}^{-1}$	7.3	0.07	$^\circ\,\mathrm{K}^{-1}$	2.7		
			79	0.18	$^\circ\,\mathrm{K}^{-1}$	7.6	0.07	$^\circ\,\mathrm{K}^{-1}$	3		
[68]	WPD	$\mathrm{abs}(Z)$	630	11.8	$\mu\Omega\,\mathrm{K}^{-1}$	0.85	1.5	$\mu\Omega\,\mathrm{K}^{-1}$	0.11	23	?/NMC
[86]	Exp	f_{int}	–[f]	119.7	$\mathrm{Hz\,K}^{-1}$	8.4	32.5	$\mathrm{Hz\,K}^{-1}$	2.3	2.6	?/?
[87]	WPD	$\mathrm{Re}(Z)$	15000	–	–	–	63.8	$\mu\Omega\,\mathrm{K}^{-1}$	0.2	3.2	?/LFP
[88]	WPD	$\arg(Z)$	200	0.5	$^\circ\,\mathrm{K}^{-1}$	8.2	–	–	–	2.5	GSi/NCA
				0.46	$^\circ\,\mathrm{K}^{-1}$	7.1	–	–	–	3	GSi/NCA
				0.41	$^\circ\,\mathrm{K}^{-1}$	7.3	–	–	–	3.2	G/NCA
				0.11	$^\circ\,\mathrm{K}^{-1}$	4	–	–	–	1.3	LTO/?
				0.3	$^\circ\,\mathrm{K}^{-1}$	4.9	–	–	–	1.1	G/LFP
				0.37	$^\circ\,\mathrm{K}^{-1}$	4.7	–	–	–	2.15	G/LCO
[89]	Fit	$\arg(Z)$	10	0.57	$^\circ\,\mathrm{K}^{-1}$	5.1	0.23	$^\circ\,\mathrm{K}^{-1}$	2.1	3.2	?/NCA

(*continued on next page*)

Table A.1 (*continued*).

Ref.	Data Source	$\mathcal{Z}$	f Hz	$\lvert S_{\mathcal{Z},T_1}\rvert$		$\lvert S_{\mathcal{Z},T_1\,n}\rvert$ % K^{-1}	$\lvert S_{\mathcal{Z},T_2}\rvert$		$\lvert S_{\mathcal{Z},T_2\,n}\rvert$ % K^{-1}	Q Ah	Neg/Pos
[18]	WPD	arg (Z)	32	–	–	–	0.23	° K^{-1}	3	3.24	G/NMC
				–	–	–	0.1	° K^{-1}	2	3.3	G/NCA
				–	–	–	0.16	° K^{-1}	2.1	3.4	GSi/NCA
[90]	Fit	arg (Z)	10	0.39	° K^{-1}	14.3	0.05	° K^{-1}	1.7	2.6	?/?
			100	0.17	° K^{-1}	6.5	0.07	° K^{-1}	2.6		
			1000	0.12	° K^{-1}	16.8	0.03	° K^{-1}	4.6		
[91]	WPD	arg (Z)	40	0.57	° K^{-1}	8.9	0.28	° K^{-1}	4.3	70	?/NMC
[92]	WPD	Im (Z)	263	121	µΩ K^{-1}	4.7	75	µΩ K^{-1}	2.9	2	G/NMC
[24]	WPD	Im (Z)	200	227	µΩ K^{-1}	5	99	µΩ K^{-1}	2.2	2.8	?/LCO
[93]	WPD	Re (Z)	100	–	–	–	45	µΩ K^{-1}	1	3.6	G/NMC
[94]	WPD	arg (Z)	619	0.28	° K^{-1}	2.8	0.42	° K^{-1}	4.1	12	?/NMC
			620	0.25	° K^{-1}	20	0.19	° K^{-1}	15.3	3.5	?/NCA
[95]	Fit	abs (Z)	0.15	38	µΩ K^{-1}	2.9	17.7	µΩ K^{-1}	1.3	50	?/NMC
[96]	WPD	abs (Z)	5	–	–	–	14	µΩ K^{-1}	1.3	50	?/NMC
[4]	Fit	Im (Z)	100	431	µΩ K^{-1}	5.2	224	µΩ K^{-1}	2.7	3	?/NMC
[97]	Fit	arg (Z)	136	0.26	° K^{-1}	2.7	0.26	° K^{-1}	2.7	11	G/NMC
[16]	WPD	abs (Z)	1000	–	–	–	53	µΩ K^{-1}	0.3	2.6	G/NMC
		arg (Z)		–	–	–	0.2	° K^{-1}	26.4		
[98]	WPD	abs (Z)	10	47	µΩ K^{-1}	3.5	11.5	µΩ K^{-1}	0.9	70	?/NMC
		arg (Z)		0.6	° K^{-1}	5.1	0.32	° K^{-1}	2.7		
[99]	Fit	abs (Z)	10	33	µΩ K^{-1}	6.7	5	µΩ K^{-1}	1	120	?/?
		arg (Z)	17.5	0.71	° K^{-1}	11.9	0.31	° K^{-1}	5.2		
[22]	WPD	Im (Z)	631	78	µΩ K^{-1}	7	64	µΩ K^{-1}	5.8	4.9	GSi/NCA
[100]	Fit	Im (Z)	400	365	µΩ K^{-1}	12.9	64	µΩ K^{-1}	2.3	3.45	?/NCA
			800	316	µΩ K^{-1}	19.9	36	µΩ K^{-1}	2.3		
			1250	121	µΩ K^{-1}	16.2	59	µΩ K^{-1}	7.9		
	WPD		50	122	µΩ K^{-1}	5.3	59	µΩ K^{-1}	2.5		
[101]	Fit	Im (Z)	100	541	µΩ K^{-1}	4.2	382	µΩ K^{-1}	2.9	1.8	?/LFP
[102]	Exp	arg (Z)	957	0.13	° K^{-1}	4.1	0.1	° K^{-1}	3.2	1.8	G/LFP
				0.15	° K^{-1}	1.5	0.17	° K^{-1}	1.7	1.5	HC/NaLO
			1000	0.12	° K^{-1}	645	0.07	° K^{-1}	348	1.25	HC/NaLO
[103]	Fit	Im (Z)	600	158	µΩ K^{-1}	4.2	99	µΩ K^{-1}	2.6	1.8	G/LFP
			800	133	µΩ K^{-1}	4.3	85	µΩ K^{-1}	2.7		
			1000	116	µΩ K^{-1}	4.5	75	µΩ K^{-1}	2.9		
[104]	WPD	arg (Z)	87	0.34	° K^{-1}	8.4	0.18	° K^{-1}	4.4	3.35	?/NMC
[64]	WPD	arg (Z)	720	0.2	° K^{-1}	5.7	0.21	° K^{-1}	5.9	2.55	G/NMC
[105]	WPD	arg (Z)	760	0.21	° K^{-1}	3.2	0.09	° K^{-1}	1.4	4.9	G/NMC
[106]	Exp	Re (Z)	8	27.8	µΩ K^{-1}	3.5	5	µΩ K^{-1}	0.6	116	G/NMC
This work	Exp	arg (Z)	1000	0.21	° K^{-1}	7.9	0.13	° K^{-1}	4.9	3.5	GSi/NMC
				0.34	° K^{-1}	6.2	0.31	° K^{-1}	5.7	1.2	G/LFP
				0.27	° K^{-1}	16.4	0.24	° K^{-1}	14.6	4.5	GSi/LFP
				0.19	° K^{-1}	6.2	0.15	° K^{-1}	4.9	3.5	GSi/NMC
			646	0.15	° K^{-1}	1.6	0.18	° K^{-1}	1.8	1.3	HC/NaLO
			500	0.31	° K^{-1}	2	0.23	° K^{-1}	1.5	75	G/NMC

[a] 0.68 kHz to 6 kHz.
[b] 0.27 kHz to 1.7 kHz.
[c] Non-zero intercept frequency.
[d] 1.6 kHz and 2 kHz.
[e] 0.3 kHz to 2.7 kHz.
[f] 0.7 kHz to 7.3 kHz.

Appendix C. EV powertrain parameters

See Table C.1.

Table B.1
Dataset B: Summary of Electrochemical Impedance Spectroscopy (EIS) data used to determine the optimal measurement frequency for internal cell temperature estimation. The operating point for each cell, including State of Charge (SoC), State of Health (SoH), and temperature (T), is provided. The nominal cell capacity Q in Ah and the negative/positive electrode active materials (Neg/Pos) are also provided. Data sources are indicated in the second column, where 'Exp' denotes experimental data and 'WPD' denotes the use of the WebPlotDigitizer tool [45] for data extraction from graphical plots. The publications are listed in chronological order, with the earliest publication date first. Data marked with '?' indicates information that was not reported in the original studies.

Reference	Data Source	SoC %	SoH %	T °C	Q Ah	Form Factor	Neg/Pos
[112]	Exp	60	100	30	20	Pouch	G/NMC
[27]	Exp	60	100	30	7.5	Cylindrical	G/NCA
[78]	WPD	50	100	23	8	Prismatic	?/LFP
[30]	Exp	60	100	30	90	Prismatic	G/LFP
[113]	Exp	60	100	30	12	Pouch	G/NCA
[114]	Exp	50	100	35	20	Pouch	G/NMC
					5		LTO/NCA
					14		G/LFP
[89]	WPD	50	100	25	3.2	Cylindrical	?/NCA
[115]	Exp	100	100	20	2.5	Cylindrical	GSi/NCA
[116]	Exp	50	100	22	3	Cylindrical	GSi/NCA
[117]	Exp	50	100	23	3	Cylindrical	G/NMC
[118]	Exp	100	100	25	3.5	Cylindrical	?/NCA
					3.5		GSi/NMC
					2.5		GSi/NCA
[119]	Exp	50	100	25	50	Prismatic	G/NMC
[120]	Exp	50	100	25	5	Cylindrical	?/NMC
[121]	Exp	50	100	25	3.25	Cylindrical	?/NCA
[93]	Exp	50	100	26	3.6	Pouch	G/NMC
[122]	WPD	50	100	25	3.2	Cylindrical	?/NMC
[94]	Exp	50	100	30	3.5	Cylindrical	?/NCA
					12	Pouch	?/NMC
[123]	Exp	50	100	25	1	Pouch	G/NMC
[124]	Exp	50	100	25	1.2	Cylindrical	HC/NaLO
[23]	Exp	55	100	25	3	Cylindrical	G/NMC
[99]	WPD	50	100	25	120	Prismatic	?/?
[22]	WPD	50	100	25	4.9	Cylindrical	GSi/NCA
					4.2		GSi/NCA
[125]	Exp	50	100	25	3	Cylindrical	GSi/NMC
[126]	Exp	50	100	25	0.7	Cylindrical	HC/NaLO
[102]	Exp	45	100	25	1.5	Cylindrical	HC/NaLO
					1.25		HC/NaLO
					1.8		G/LFP
[127]	Exp	50	100	20	0.6	Cylindrical	G/LFP
[21]	Exp	50	100	23	4.2	Cylindrical	G/NMC
[128]	Exp	60	100	25	58	Prismatic	G/NMC
[106]	Exp	50	100	20	116	Prismatic	G/NMC
[129]	Exp	50	100	25	32	Prismatic	?/LFP
This work	Exp	50	90	20	3.5	Cylindrical	GSi/NMC
			100		1.2		G/LFP
				25	1.3		HC/NaLO
					4.5		GSi/NMC
					3.5		GSi/NMC
				25	75		G/NMC

Table C.1
Overview of powertrain parameters of 60 Electric Vehicles (EVs). The switching frequency of the traction inverter is represented by f_{sw}. The maximum frequency of the electric motor control signal, generated by the traction inverter and denoted as $f_{el,max}$, is calculated using Eq. (6), using the maximum revolutions per minute (RPM_{max}) and the number of pole pairs (N_P). Both, the traction inverter switching frequency and the motor control signal, are present in the battery current and can disturb an Electrochemical Impedance Spectroscopy (EIS) measurement, as $f_{el,max}$ can reach up to 1.4 kHz.

Reference	Brand	Model	Year	f_{sw} kHz	RPM_{max} min^{-1}	N_P	$f_{el,max}$ Hz
[130]	Aion	650 Zhihao	2024	–	13900	6	695
[130]	Aito	M9	2024	–	17582	6	879
[130]	Arcfox	Alpha-S	2022	–	16225	6	811
[131]	Audi	e-tron	–	16	16000	8	1067
[130]	Avatr	12	2024	–	17435	6	872
[131]	BMW	i3	–	12	11400	8	760
[130]	BMW	i5 M60 xDrive	2023	–	16289	6	815
[130]	BMW	iX xDrive 40	2022	–	14949	6	748
[130]	BYD	Dolphin Knight Edition	2021	–	13220	8	881
[130]	BYD	Han AWD	2020	–	15014	8	1000
[130]	BYD	Qin Pro	2020	–	11100	8	740
[130]	BYD	Seagull	2023	–	11050	10	921
[130]	BYD	Shark GS	2025	–	12240	8	816
[130]	BYD	Song Plus 520	2024	–	12847	8	856
[130]	BYD	Yuan Plus	2022	–	12630	8	842
[131]	Chevrolet	Bolt EV	2016	10	10000	8	667
[132]	Citroën	C-Zero	2010	7.1	8800	4	587
[130]	Citroën	E-C3 Max	2024	–	16960	8	1130
[130]	Citroën	E-C4 Feel Pack	2020	–	11177	8	745
[130]	Dacia	Spring Electric Plus	2021	–	11150	8	743
[130]	Denza	N7 Long Max	2023	–	14180	8	945
[130]	Fiat	E-Ducato	2024	–	11300	8	753
[130]	Fisker	Ocean One	2023	–	15778	8	1053
[131,133]	Ford	Mustang Mach-E AWD	2020	15	13800	8	920
[130]	Geely	Galaxy E5 530	2023	–	14700	8	980
[130]	Great Wall Motor	Pao	2021	–	8801	8	587
[130]	Hozon	Neta Aya	2023	–	9566	8	638
[130]	Hyundai	Creta Electric LR	2025	–	12600	8	840
[130]	Hyundai	Ioniq 6 First Edition	2023	–	12800	8	853
[131]	Hyundai	Kona Electric	–	10	12000	8	800
[130]	IM Motors	L7 Pro	2022	–	14710	6	736
[130]	Kia	EV5 530 Land	2023	–	12200	8	813
[130]	Maxus	Deliver 9 LH	2020	–	13300	8	887
[130]	Mercedes	EQS 580 4Matic	2022	10	13638	8	909
[130]	MG	4	2022	–	13384	8	892
[130]	MG	ZS	2022	–	10300	8	687
[130]	Nio	ES6	2020	–	11866	8	791
[130]	Nissan	Ariya B6	2022	–	15700	8	1047
[131]	Nissan	Leaf	–	10	10000	8	667
[130]	Ora	Good Cat LR	2021	–	12800	8	853
[130]	Porsche	Macan EV Turbo	2024	–	13200	8	880
[131]	Porsche	Taycan	–	20	20000	8	1333
[130]	Renault	R5 E-Tech Electric Iconic Five	2024	–	11900	8	793
[130]	Renault	Megane E-Tech EV60	2022	–	11500	8	767
[130]	Renault	Zoe R135 Z.E. 50	2020	–	11350	4	378
[134]	Rivian	R1T	2023	–	16128	8	1075
[135]	Tesla	Cybertruck Single/Dual Motor	2024	–	16328	6	816
[135]	Tesla	Cybertruck Tri Motor	2024	–	18973	6	949
[130]	Tesla	Model 3 LR	2023	–	17225	6	861
[131]	Tesla	Model S	2022	20	18000	8	1200
[136]	Tesla	Model S Plaid	2022	–	18031	6	902
[130]	Tesla	Model Y LR AWD	2022	–	15300	6	765
[130]	Toyota	bZ4X AWD	2023	–	14250	8	950
[130]	Volvo	EX30 Ultra	2024	–	13000	8	867
[130]	VW	ID.3	2021	–	13692	8	931
[130]	VW	ID.6 X	2021	–	16800	8	1120
[130]	VW	ID Buzz	2023	–	14300	8	953
[130]	Xiaomi	SU7 Max	2024	–	15900	8	1060
[130]	XPeng	G6 Performance Max	2023	–	12300	6	615
[130]	XPeng	G9 Max	2022	–	16200	8	1080

Appendix D. Supplementary data

Supplementary material related to this article can be found online at https://doi.org/10.1016/j.jpowsour.2025.239111.

Data availability

All data used in this article are publicly available through Mendeley Data repositories: Dataset A, Dataset B, and measured EIS data at https://doi.org/10.17632/zdpxdkx6rn.1; Measured traction current data from the Citroën C-Zero at https://doi.org/10.17632/562fxrn7js.1.

References

[1] N. Rosenberger, P. Rosner, P. Bilfinger, J. Schöberl, O. Teichert, J. Schneider, K. Abo Gamra, C. Allgäuer, B. Dietermann, M. Schreiber, M. Ank, T. Kröger, A. Köhler, M. Lienkamp, Quantifying the state of the art of electric powertrains in battery electric vehicles: Comprehensive analysis of the tesla model 3 on the vehicle level, World Electr. Veh. J. 15 (6) (2024) 268, http://dx.doi.org/10.3390/wevj15060268.

[2] S.S. Bhoir, G. Thenaisie, C. Brivio, M. Paolone, Li-ion cells internal temperature estimation using medium-frequency measurements of impedance argument, J. Energy Storage 97 (2024) 112754, http://dx.doi.org/10.1016/j.est.2024.112754.

[3] Y. Wu, X. Long, J. Lu, R. Zhou, L. Liu, Y. Wu, Long-life in-situ temperature field monitoring using Fiber Bragg grating sensors in electromagnetic launch high-rate hardcase lithium-ion battery, J. Energy Storage 57 (2023) 106207, http://dx.doi.org/10.1016/j.est.2022.106207.

[4] Z. Chen, Y. Zhang, R. Yang, C. Liu, G. Chen, Online internal temperature estimation for lithium-ion batteries using the suppressed second–harmonic current in single–phase DC/AC converters, IEEE Trans. Ind. Electron. (2023) 1–10, http://dx.doi.org/10.1109/TIE.2023.3331090.

[5] Y. Yu, T. Vincent, J. Sansom, D. Greenwood, J. Marco, Distributed internal thermal monitoring of lithium ion batteries with fibre sensors, J. Energy Storage 50 (2022) 104291, http://dx.doi.org/10.1016/j.est.2022.104291.

[6] R.R. Richardson, S. Zhao, D.A. Howey, On-board monitoring of 2-D spatially-resolved temperatures in cylindrical lithium-ion batteries: Part II. State estimation via impedance-based temperature sensing, J. Power Sources 327 (2016) 726–735, http://dx.doi.org/10.1016/j.jpowsour.2016.06.104.

[7] C. Zhang, K. Li, J. Deng, Real-time estimation of battery internal temperature based on a simplified thermoelectric model, J. Power Sources 302 (2016) 146–154, http://dx.doi.org/10.1016/j.jpowsour.2015.10.052.

[8] T. Waldmann, G. Bisle, B.-I. Hogg, S. Stumpp, M.A. Danzer, M. Kasper, P. Axmann, M. Wohlfahrt-Mehrens, Influence of cell design on temperatures and temperature gradients in lithium-ion cells: An in operando study, J. Electrochem. Soc. 162 (6) (2015) A921–A927, http://dx.doi.org/10.1149/2.0561506jes.

[9] G. Zhang, L. Cao, S. Ge, C.-Y. Wang, C.E. Shaffer, C.D. Rahn, In situ measurement of radial temperature distributions in cylindrical Li-ion cells, J. Electrochem. Soc. 161 (10) (2014) A1499–A1507, http://dx.doi.org/10.1149/2.0051410jes.

[10] R.R. Richardson, P.T. Ireland, D.A. Howey, Battery internal temperature estimation by combined impedance and surface temperature measurement, J. Power Sources 265 (2014) 254–261, http://dx.doi.org/10.1016/j.jpowsour.2014.04.129.

[11] J.P. Schmidt, S. Arnold, A. Loges, D. Werner, T. Wetzel, E. Ivers-Tiffée, Measurement of the internal cell temperature via impedance: Evaluation and application of a new method, J. Power Sources 243 (2013) 110–117, http://dx.doi.org/10.1016/j.jpowsour.2013.06.013.

[12] C. Veth, D. Dragicevic, C. Merten, Thermal characterizations of a large-format lithium ion cell focused on high current discharges, J. Power Sources 267 (2014) 760–769, http://dx.doi.org/10.1016/j.jpowsour.2014.05.139.

[13] Z. Wang, X. Wu, Z. Bai, N. Yang, G. Guo, O.S. Banjoko, Enhancing fast charging performance of lithium-ion batteries: The role of operating temperature and charging rate, Electrochim. Acta 511 (2025) 145390, http://dx.doi.org/10.1016/j.electacta.2024.145390.

[14] K. Abo Gamra, P. Bilfinger, M. Schreiber, T. Kröger, C. Allgäuer, M. Lienkamp, Unlocking the full potential of electric vehicle fast-charging over lifetime through model-based aging adaptation, J. Energy Storage 99 (2024) 113361, http://dx.doi.org/10.1016/j.est.2024.113361.

[15] X.-G. Yang, C.-Y. Wang, Understanding the trilemma of fast charging, energy density and cycle life of lithium-ion batteries, J. Power Sources 402 (2018) 489–498, http://dx.doi.org/10.1016/j.jpowsour.2018.09.069.

[16] Y. Li, L. Jiang, N. Zhang, Z. Wei, W. Mei, Q. Duan, J. Sun, Q. Wang, Early warning method for thermal runaway of lithium-ion batteries under thermal abuse condition based on online electrochemical impedance monitoring, J. Energy Chem. 92 (2024) 74–86, http://dx.doi.org/10.1016/j.jechem.2023.12.049.

[17] N. Lyu, Y. Jin, R. Xiong, S. Miao, J. Gao, Real-time overcharge warning and early thermal runaway prediction of Li-ion battery by online impedance measurement, IEEE Trans. Ind. Electron. 69 (2) (2022) 1929–1936, http://dx.doi.org/10.1109/TIE.2021.3062267.

[18] P. Dong, Z. Liu, P. Wu, Z. Li, Z. Wang, J. Zhang, Reliable and early warning of lithium-ion battery thermal runaway based on electrochemical impedance spectrum, J. Electrochem. Soc. 168 (9) (2021) 090529, http://dx.doi.org/10.1149/1945-7111/ac239b.

[19] R. Srinivasan, B.G. Carkhuff, M.H. Butler, A.C. Baisden, Instantaneous measurement of the internal temperature in lithium-ion rechargeable cells, Electrochim. Acta 56 (17) (2011) 6198–6204, http://dx.doi.org/10.1016/j.electacta.2011.03.136.

[20] S. Ludwig, M. Steinhardt, A. Jossen, Determination of internal temperature differences for various cylindrical lithium-ion batteries using a pulse resistance approach, Batteries 8 (7) (2022) 60, http://dx.doi.org/10.3390/batteries8070060.

[21] S. Pohlmann, A. Mashayekh, J. Buberger, J. Estaller, A. Wiedenmann, M. Kuder, A. Neve, T. Weyh, Correlation analysis and feature extraction using impedance spectroscopy over aging of lithium ion batteries, J. Energy Storage 105 (2025) 114715, http://dx.doi.org/10.1016/j.est.2024.114715.

[22] T. Hackmann, S. Esser, M.A. Danzer, Operando determination of lithium-ion cell temperature based on electrochemical impedance features, J. Power Sources 615 (2024) 235036, http://dx.doi.org/10.1016/j.jpowsour.2024.235036.

[23] M.J. Jung, S.-G. Lee, K.-S. Choi, A new diagnostic indicator for lithium-ion batteries via electrochemical impedance spectroscopy: Harnessing the highest frequency peak in distribution of relaxation times, J. Power Sources 611 (2024) 234743, http://dx.doi.org/10.1016/j.jpowsour.2024.234743.

[24] K. Mc Carthy, H. Gullapalli, T. Kennedy, Real-time internal temperature estimation of commercial Li-ion batteries using online impedance measurements, J. Power Sources 519 (2022) 230786, http://dx.doi.org/10.1016/j.jpowsour.2021.230786.

[25] L. Wang, D. Lu, M. Song, X. Zhao, G. Li, Instantaneous estimation of internal temperature in lithium–ion battery by impedance measurement, Int. J. Energy Res. 44 (4) (2020) 3082–3097, http://dx.doi.org/10.1002/er.5144.

[26] J.G. Zhu, Z.C. Sun, X.Z. Wei, H.F. Dai, A new lithium-ion battery internal temperature on-line estimate method based on electrochemical impedance spectroscopy measurement, J. Power Sources 274 (2015) 990–1004, http://dx.doi.org/10.1016/j.jpowsour.2014.10.182.

[27] L. Raijmakers, D.L. Danilov, J. van Lammeren, M. Lammers, P. Notten, Sensorless battery temperature measurements based on electrochemical impedance spectroscopy, J. Power Sources 247 (2014) 539–544, http://dx.doi.org/10.1016/j.jpowsour.2013.09.005.

[28] W. Waag, S. Käbitz, D.U. Sauer, Experimental investigation of the lithium-ion battery impedance characteristic at various conditions and aging states and its influence on the application, Appl. Energy 102 (2013) 885–897, http://dx.doi.org/10.1016/j.apenergy.2012.09.030.

[29] S. Buller, M. Thele, R. DeDoncker, E. Karden, Impedance-based simulation models of supercapacitors and Li-ion batteries for power electronic applications, IEEE Trans. Ind. Appl. 41 (3) (2005) 742–747, http://dx.doi.org/10.1109/TIA.2005.847280.

[30] L.H.J. Raijmakers, D.L. Danilov, J.P.M. van Lammeren, T.J.G. Lammers, H.J. Bergveld, P.H.L. Notten, Non-zero intercept frequency: An accurate method to determine the integral temperature of Li-ion batteries, IEEE Trans. Ind. Electron. 63 (5) (2016) 3168–3178, http://dx.doi.org/10.1109/TIE.2016.2516961.

[31] D. Li, L. Wang, C. Duan, Q. Li, K. Wang, Temperature prediction of lithium–ion batteries based on electrochemical impedance spectrum: A review, Int. J. Energy Res. 46 (8) (2022) 10372–10388, http://dx.doi.org/10.1002/er.7905.

[32] K. Mc Carthy, H. Gullapalli, K.M. Ryan, T. Kennedy, Review—Use of impedance spectroscopy for the estimation of Li–ion battery state of charge, state of health and internal temperature, J. Electrochem. Soc. 168 (8) (2021) 080517, http://dx.doi.org/10.1149/1945-7111/ac1a85.

[33] L. Raijmakers, D.L. Danilov, R.-A. Eichel, P. Notten, A review on various temperature–Indication methods for Li–ion batteries, Appl. Energy 240 (2019) 918–945, http://dx.doi.org/10.1016/j.apenergy.2019.02.078.

[34] Y. Zheng, Y. Che, J. Guo, N.A. Weinreich, A. Kulkarni, A. Nadeem, X. Sui, R. Teodorescu, Real-time sensorless temperature estimation of lithium-ion batteries based on online operando impedance acquisition, IEEE Trans. Power Electron. (2024) 1–14, http://dx.doi.org/10.1109/TPEL.2024.3424267.

[35] H. Adenusi, G.A. Chass, S. Passerini, K.V. Tian, G. Chen, Lithium batteries and the solid electrolyte interphase (SEI)—Progress and outlook, Adv. Energy Mater. 13 (10) (2023) http://dx.doi.org/10.1002/aenm.202203307.

[36] A. Wang, S. Kadam, H. Li, S. Shi, Y. Qi, Review on modeling of the anode solid electrolyte interphase (SEI) for lithium-ion batteries, Npj Comput. Mater. 4 (1) (2018) http://dx.doi.org/10.1038/s41524-018-0064-0.

[37] E. Peled, S. Menkin, Review—SEI: Past, present and future, J. Electrochem. Soc. 164 (7) (2017) A1703–A1719, http://dx.doi.org/10.1149/2.1441707jes.

[38] E. Peled, Film forming reaction at the lithium/electrolyte interface, J. Power Sources 9 (3) (1983) 253–266, http://dx.doi.org/10.1016/0378-7753(83)87026-8.

[39] L. Ran, W. Junfeng, W. Haiying, L. Gechen, Prediction of state of charge of Lithium-ion rechargeable battery with electrochemical impedance spectroscopy theory, in: 2010 5th IEEE Conference on Industrial Electronics and Applications, IEEE, 2010, pp. 684–688, http://dx.doi.org/10.1109/ICIEA.2010.5516984.

[40] Y. Li, Z. He, M. Ye, Q. Wang, G. Lian, Y. Sun, M. Wei, A semi-supervised learning strategy for lithium-ion battery capacity estimation with limited impedance data, Energy 319 (2025) 135129, http://dx.doi.org/10.1016/j.energy.2025.135129.

[41] Z. Geng, T. Thiringer, In situ key aging parameter determination of a vehicle battery using only CAN signals in commercial vehicles, Appl. Energy 314 (2022) 118932, http://dx.doi.org/10.1016/j.apenergy.2022.118932.

[42] B. Liebhart, S. Diehl, C. Endisch, Sensitivity analysis of battery cell aging estimators based on impedance spectroscopy regarding temperature compensation, in: 2020 IEEE Conference on Control Technology and Applications, CCTA, IEEE, 2020, pp. 801–806, http://dx.doi.org/10.1109/CCTA41146.2020.9206395.

[43] Z. Xia, J.A.A. Qahouq, Adaptive and fast state of health estimation method for lithium-ion batteries using online complex impedance and artificial neural network, in: 2019 IEEE Applied Power Electronics Conference and Exposition, APEC, 2019, pp. 3361–3365, http://dx.doi.org/10.1109/APEC.2019.8721906.

[44] N. Sailer, C. Steffan, J.P. Schmidt, Dataset: Practical considerations and limitations of online EIS-based battery internal temperature estimation in traction applications, 2025, http://dx.doi.org/10.17632/zdpxdkx6rn.1, Mendeley dataset, Version 1.

[45] A. Rohatgi, WebPlotDigitizer version 5.2, 2024, URL https://automeris.io/. (Accessed 18 November 2025).

[46] F. Marin, A. Rohatgi, S. Charlot, WebPlotDigitizer, a polyvalent and free software to extract spectra from old astronomical publications: application to ultraviolet spectropolarimetry, 2017, arXiv:1708.02025. URL https://arxiv.org/abs/1708.02025.

[47] Bio-Logic SAS, SP-300 Potentiostat - BioLogic, 2025, URL https://www.biologic.net/products/sp-300/. (Accessed 18 November 2025).

[48] Bio-Logic SAS, VMP-300 Potentiostat - BioLogic, 2025, URL https://www.biologic.net/products/vmp-300/. (Accessed 18 November 2025).

[49] M. Grubmüller, B. Schweighofer, H. Wegleiter, Fast, high accuracy, freely programmable single cell battery measurement system, in: 2015 IEEE International Instrumentation and Measurement Technology Conference (I2MTC) Proceedings, IEEE, 2015, pp. 133–137, http://dx.doi.org/10.1109/I2MTC.2015.7151253.

[50] Clima Temperatur Systeme GmbH, Temperaturprüfschränke der Baureihe T - CTS Umweltsimulation, 2025, URL https://www.cts-umweltsimulation.at/produkt/temperaturpruefschrank/. (Accessed 18 November 2025).

[51] HIOKI E.E. Corporation, HIOKI Clamp On Probe 3275: Wideband Current Probe for Oscilloscopes, 2025, URL https://www.hioki.com/euro-en/products/current-probes/wide-band/id_5988. (Accessed 18 November 2025).

[52] Pico Technology Ltd., PicoScope® 5000 Series FlexRes® Oscilloscopes, 2025, URL https://www.picotech.com/oscilloscope/5000/flexible-resolution-oscilloscope. (Accessed 18 November 2025).

[53] N. Sailer, C. Steffan, A. Thaler, A. Tengg, Citroen C zero traction currents, 2025, http://dx.doi.org/10.17632/562fxrn7js.1, Mendeley dataset, Version 1.

[54] R. Srinivasan, P.A. Demirev, B.G. Carkhuff, Rapid monitoring of impedance phase shifts in lithium-ion batteries for hazard prevention, J. Power Sources 405 (2018) 30–36, http://dx.doi.org/10.1016/j.jpowsour.2018.10.014.

[55] S. Baazouzi, N. Feistel, J. Wanner, I. Landwehr, A. Fill, K.P. Birke, Design, properties, and manufacturing of cylindrical Li-ion battery cells—A generic overview, Batteries 9 (6) (2023) 309, http://dx.doi.org/10.3390/batteries9060309.

[56] S. Li, M.W. Marzook, C. Zhang, G.J. Offer, M. Marinescu, How to enable large format 4680 cylindrical lithium-ion batteries, Appl. Energy 349 (2023) 121548, http://dx.doi.org/10.1016/j.apenergy.2023.121548.

[57] A. Frank, J. Sturm, M. Steinhardt, A. Rheinfeld, A. Jossen, Impact of current collector design and cooling topology on fast charging of cylindrical lithium-ion batteries, ECS Adv. 1 (4) (2022) 040502, http://dx.doi.org/10.1149/2754-2734/ac97e0.

[58] J. Sturm, A. Frank, A. Rheinfeld, S.V. Erhard, A. Jossen, Impact of electrode and cell design on fast charging capabilities of cylindrical lithium-ion batteries, J. Electrochem. Soc. 167 (13) (2020) 130505, http://dx.doi.org/10.1149/1945-7111/abb40c.

[59] S. Stock, J. Hagemeister, S. Grabmann, J. Kriegler, J. Keilhofer, M. Ank, J.L. Dickmanns, M. Schreiber, F. Konwitschny, N. Wassiliadis, M. Lienkamp, R. Daub, Cell teardown and characterization of an automotive prismatic LFP battery, Electrochim. Acta 471 (2023) 143341, http://dx.doi.org/10.1016/j.electacta.2023.143341.

[60] P. Taheri, A. Mansouri, B. Schweitzer, M. Yazdanpour, M. Bahrami, Electrical constriction resistance in current collectors of large-scale lithium-ion batteries, J. Electrochem. Soc. 160 (10) (2013) A1731–A1740, http://dx.doi.org/10.1149/2.041310jes.

[61] J. Gorsch, J. Schneiders, M. Frieges, N. Kisseler, D. Klohs, H. Heimes, A. Kampker, M. Muñoz Castro, E. Siebecke, Contrasting a BYD Blade prismatic cell and Tesla 4680 cylindrical cell with a teardown analysis of design and performance, Cell Rep. Phys. Sci. 6 (3) (2025) 102453, http://dx.doi.org/10.1016/j.xcrp.2025.102453.

[62] J.B. Quinn, T. Waldmann, K. Richter, M. Kasper, M. Wohlfahrt-Mehrens, Energy density of cylindrical Li-ion cells: A comparison of commercial 18650 to the 21700 cells, J. Electrochem. Soc. 165 (14) (2018) A3284–A3291, http://dx.doi.org/10.1149/2.0281814jes.

[63] T.F. Landinger, G. Schwarzberger, A. Jossen, High frequency impedance characteristics of cylindrical lithium-ion cells: Physical-based modeling of cell state and cell design dependencies, J. Power Sources 488 (2021) 229463, http://dx.doi.org/10.1016/j.jpowsour.2021.229463.

[64] J. Li, T. Li, Y. Qiao, Z. Tan, X. Qiu, H. Deng, W. Li, X. Qi, W. Wu, Internal temperature estimation method for lithium-ion battery based on multi-frequency imaginary part impedance and GPR model, J. Energy Storage 118 (2025) 116287, http://dx.doi.org/10.1016/j.est.2025.116287.

[65] N.S. Spinner, C.T. Love, S.L. Rose-Pehrsson, S.G. Tuttle, Expanding the operational limits of the single-point impedance diagnostic for internal temperature monitoring of lithium-ion batteries, Electrochim. Acta 174 (2015) 488–493, http://dx.doi.org/10.1016/j.electacta.2015.06.003.

[66] U. Westerhoff, K. Kurbach, F. Lienesch, M. Kurrat, Analysis of lithium-ion battery models based on electrochemical impedance spectroscopy, Energy Technol. 4 (12) (2016) 1620–1630, http://dx.doi.org/10.1002/ente.201600154.

[67] A. Straßer, A. Adam, J. Li, In operando detection of Lithium plating via electrochemical impedance spectroscopy for automotive batteries, J. Power Sources 580 (2023) 233366, http://dx.doi.org/10.1016/j.jpowsour.2023.233366.

[68] H. Beelen, K. Mundaragi Shivakumar, L. Raijmakers, M. Donkers, H.J. Bergveld, Towards impedance–based temperature estimation for Li–ion battery packs, Int. J. Energy Res. 44 (4) (2020) 2889–2908, http://dx.doi.org/10.1002/er.5107.

[69] H. Ito, Y. Nishimura, L. Lin, M. Fukui, An accurate assembled battery impedance measurement system and its evaluation, in: 2020 RISP International Workshop on Nonlinear Circuits, Communications and Signal Processing, NCSP 2020, 2020.

[70] S. Zhang, Z. Wei, L. Zhang, J. Hu, R. Dai, Equivalent sampling-enabled module-level battery impedance measurement for in-situ lithium plating diagnostic, J. Power Sources 600 (2024) 234239, http://dx.doi.org/10.1016/j.jpowsour.2024.234239.

[71] I.T. AG, High voltage traction inverter application presentation, 2024, URL https://www.infineon.com/dgdl/Infineon-Infineon_High_voltage_traction_inverter_presentation-ApplicationPresentation-v05_00-EN.pdf?fileId=8ac78c8c8afe5bd0018b291672a47e70. (Accessed 18 November 2025).

[72] D.-Y. Kim, Analysis of efficiency and noise, vibration, and hardness characteristics of inverter for electric vehicles according to pulse width modulation technique, World Electr. Veh. J. 15 (12) (2024) 546, http://dx.doi.org/10.3390/wevj15120546.

[73] M. Sarrazin, K. Janssens, H. van der Auweraer, Virtual car sound synthesis approach for hybrid and electric vehicles, in: Euronoise 2012: 9th European Conference on Noise Control, 2012, URL https://www.researchgate.net/publication/292991580_Virtual_Car_Sound_Synthesis_Approach_for_Hybrid_and_Electric_Vehicles.

[74] D. Andre, M. Meiler, K. Steiner, C. Wimmer, T. Soczka-Guth, D.U. Sauer, Characterization of high-power lithium-ion batteries by electrochemical impedance spectroscopy. I. Experimental investigation, J. Power Sources 196 (12) (2011) 5334–5341, http://dx.doi.org/10.1016/j.jpowsour.2010.12.102.

[75] R. Srinivasan, A. Carson Baisden, B.G. Carkhuff, M.H. Butler, The five modes of heat generation in a Li-ion cell under discharge, J. Power Sources 262 (2014) 93–103, http://dx.doi.org/10.1016/j.jpowsour.2014.03.062.

[76] R. Srinivasan, L. Srinivasan, Graphitic carbon anode temperature excursions reflect crystallographic phase transitions in lithium-ion cells, J. Power Sources 293 (2015) 876–882, http://dx.doi.org/10.1016/j.jpowsour.2015.06.017.

[77] R. Schwarz, K. Semmler, M. Wenger, V.R.H. Lorentz, M. Marz, Sensorless battery cell temperature estimation circuit for enhanced safety in battery systems, in: IECON 2015 - 41st Annual Conference of the IEEE Industrial Electronics Society, 2015, 001536–001541, http://dx.doi.org/10.1109/IECON.2015.7392319.

[78] X. Wang, X. Wei, H. Dai, Q. Wu, State estimation of lithium ion battery based on electrochemical impedance spectroscopy with on-board impedance measurement system, in: 2015 IEEE Vehicle Power and Propulsion Conference, VPPC, 2015, pp. 1–5, http://dx.doi.org/10.1109/VPPC.2015.7353021.

[79] J. Zhu, Z. Sun, X. Wei, H. Dai, Battery internal temperature estimation for LiFePO4 battery based on impedance phase shift under operating conditions, Energies 10 (1) (2017) 60, http://dx.doi.org/10.3390/en10010060.

[80] P. Haussmann, J. Melbert, Internal cell temperature measurement and thermal modeling of lithium ion cells for automotive applications by means of electrochemical impedance spectroscopy, SAE Int. J. Altern. Powertrains 6 (2) (2017) 261–270, http://dx.doi.org/10.4271/2017-01-1215.

[81] B.M. Huhman, A Single-Frequency Impedance Diagnostic for State of Health Determination in Li-ion 4P1S Battery Packs (Ph.D. thesis), Virginia Polytechnic Institute and State University, 2017, URL http://hdl.handle.net/10919/80573. (Accessed 18 November 2025).

[82] M. Ranieri, D. Alberto, H. Piret, V. Cattin, Electronic module for the thermal monitoring of a Li-ion battery cell through the electrochemical impedance estimation, Microelectron. Reliab. 79 (2017) 410–415, http://dx.doi.org/10.1016/j.microrel.2017.06.010.

[83] J.-q. Li, L. Fang, W. Shi, X. Jin, Layered thermal model with sinusoidal alternate current for cylindrical lithium-ion battery at low temperature, Energy 148 (2018) 247–257, http://dx.doi.org/10.1016/j.energy.2018.01.024.

[84] C. Love, M. Dubarry, T. Reshetenko, A. Devie, N. Spinner, K. Swider-Lyons, R. Rocheleau, Lithium-ion cell fault detection by single-point impedance diagnostic and degradation mechanism validation for series-wired batteries cycled at 0 °C, Energies 11 (4) (2018) 834, http://dx.doi.org/10.3390/en11040834.

[85] X. Wang, X. Wei, Q. Chen, J. Zhu, H. Dai, Lithium-ion battery temperature on-line estimation based on fast impedance calculation, J. Energy Storage 26 (2019) 100952, http://dx.doi.org/10.1016/j.est.2019.100952.

[86] A.A. Hussein, A.A. Fardoun, An adaptive sensorless measurement technique for internal temperature of Li-ion batteries using impedance phase spectroscopy, IEEE Trans. Ind. Appl. 56 (3) (2020) 3043–3051, http://dx.doi.org/10.1109/TIA.2020.2979783.

[87] C. Gonzalez Moral, D. Fernandez, J.M. Guerrero, D. Reigosa, C. Riva, F. Briz, Thermal monitoring of LiFePO4 batteries using switching harmonics, IEEE Trans. Ind. Appl. (2020) 1, http://dx.doi.org/10.1109/TIA.2020.2988425.

[88] A. Fly, I. Kirkpatrick, R. Chen, Low temperature performance evaluation of electrochemical energy storage technologies, Appl. Therm. Eng. 189 (2021) 116750, http://dx.doi.org/10.1016/j.applthermaleng.2021.116750.

[89] F. Wenjie, Z. Zhibin, D. Ming, R. Ming, On-line estimation method for internal temperature of lithium-ion battery based on electrochemical impedance spectroscopy, in: 2021 IEEE Electrical Insulation Conference, EIC, IEEE, 2021, pp. 247–251, http://dx.doi.org/10.1109/EIC49891.2021.9612262.

[90] A.A. Hussein, A.A. Fardoun, An effective impedance-phase method for sensorless measurement of Li-ion battery cells' internal temperature, in: 2021 IEEE Energy Conversion Congress and Exposition, ECCE, IEEE, 2021, pp. 5899–5902, http://dx.doi.org/10.1109/ECCE47101.2021.9595234.

[91] S.E. Ezahedi, S. Park, S. Jo, C. Lee, J. Kim, Electrochemical impedance spectroscopy based Internal temperature estimation for 10 high capacity lithium-ion battery cells with initial manufacturing deviation using Pattern recognition methods, in: Power Electronics Conference, Seoul, 2021, pp. 131–133, URL https://www.dbpia.co.kr/Journal/articleDetail?nodeId=NODE10756901. (Accessed 18 November 2025).

[92] K. Ouyang, Y. Fan, M. Yazdi, W. Peng, Data–driven–based internal temperature estimation for lithium–Ion battery under variant state–of–charge via electrochemical impedance spectroscopy, Energy Technol. 10 (3) (2022) http://dx.doi.org/10.1002/ente.202100910.

[93] I. Lalinde, A. Berrueta, A. Soto, J. Arza, P. Sanchis, A. Ursúa, Temperature indicators and overtemperature detection in lithium-ion batteries based on electrochemical impedance spectroscopy, in: 2023 IEEE 32nd International Symposium on Industrial Electronics, ISIE, 2023, http://dx.doi.org/10.1109/ISIE51358.2023.10228079.

[94] S. Bhoir, G. Thenaisie, M. Paolone, Li-ion battery internal temperature estimation using electrochemical impedance spectroscopy, in: 2023 International Conference on Clean Electrical Power, ICCEP, IEEE, 2023, pp. 13–19, http://dx.doi.org/10.1109/ICCEP57914.2023.10247457.

[95] Y. Zheng, N.A. Weinreich, A. Kulkarni, Y. Che, H. Sorouri, X. Sui, R. Teodorescu, Sensorless state of temperature estimation for smart battery based on electrochemical impedance, in: 2023 25th European Conference on Power Electronics and Applications, EPE'23 ECCE Europe, IEEE, 2023, pp. 1–8, http://dx.doi.org/10.23919/EPE23ECCEEurope58414.2023.10264452.

[96] Y. Zheng, N.A. Weinreich, A. Kulkarni, X. Sui, R. Teodorescu, Sensorless temperature estimation for lithium-ion batteries via online impedance acquisition, in: Energy Storage Conference 2023, ESC 2023, Institution of Engineering and Technology, 2023, pp. 53–57, http://dx.doi.org/10.1049/icp.2023.3103.

[97] R. Yang, K. Li, Y. Xie, Y. Fan, B. Liu, Z. Deng, A phase-based method for estimating the internal temperature of solid-state battery, J. Energy Storage 85 (2024) 111007, http://dx.doi.org/10.1016/j.est.2024.111007.

[98] S.E. Ezahedi, M. Kharrich, J. Kim, Multi-cell sensorless internal temperature estimation based on electrochemical impedance spectroscopy with Gaussian process regression for lithium-ion batteries safety, J. Energy Storage 94 (2024) 112467, http://dx.doi.org/10.1016/j.est.2024.112467.

[99] Jingjing. Lei, Zehao. Li, Binbin. Chen, Denggao. Huang, Estimation of internal battery temperature based on electrochemical impedance spectroscopy, Energy Storage Sci. Technol. 13 (8) (2024) http://dx.doi.org/10.19799/j.cnki.2095-4239.2024.0134.

[100] Z. Zhao, H. Hu, Z. He, H.H.-C. Iu, P. Davari, F. Blaabjerg, H. Wang, Online temperature estimation for lithium-ion batteries utilizing a single-frequency impedance unaffected by their peripheral circuits, IEEE Trans. Power Electron. (2024) 1–17, http://dx.doi.org/10.1109/TPEL.2024.3437159.

[101] A. Yuan, T. Cai, H. Luo, Z. Song, B. Wei, Core temperature estimation of lithium-ion battery based on numerical model fusion deep learning, J. Energy Storage 102 (2024) 114148, http://dx.doi.org/10.1016/j.est.2024.114148.

[102] M. Rehm, M. Fischer, M.R. Gomez, M. Schütte, D.U. Sauer, A. Jossen, Comparing the electrical performance of commercial sodium-ion and lithium-iron-phosphate batteries, J. Power Sources 633 (2025) 236290, http://dx.doi.org/10.1016/j.jpowsour.2025.236290.

[103] A. Geng, H. Hu, J. Chen, Y. Ge, Z. He, Impedance-based online internal temperature estimation for lithium-ion batteries considering the parasitic parameters of power wires, IEEE Trans. Power Electron. (2025) 1–5, http://dx.doi.org/10.1109/TPEL.2025.3531014.

[104] L.-R. Chen, S.-H. Wei, H.-Y. Hsieh, H.-Y. Shen, C.-H. Wu, Estimation of battery internal temperature using electrochemical impedance spectroscopy, Int. J. Electrochem. Sci. (2025) http://dx.doi.org/10.1016/j.ijoes.2025.101070.

[105] V.M. Tingbari, O.I. Ekuewa, A. Nagar, A. Abbas, J. Umar, Y. Zhang, W. Na, J. Kim, Machine learning approach for accurate lithium-ion battery temperature prediction using electrochemical features independent of battery SOC and SOH, in: 2025 IEEE Applied Power Electronics Conference and Exposition, APEC, IEEE, 2025, pp. 2973–2980, http://dx.doi.org/10.1109/APEC48143.2025.10977233.

[106] J. Schöberl, J. Schumacher, R. Urban, M. Lienkamp, Impedance-based thermal runaway detection and temperature estimation for single and parallel connected large-format automotive lithium-ion batteries, ETransportation 25 (2025) 100424, http://dx.doi.org/10.1016/j.etran.2025.100424.

[107] D. Xiang, C. Yang, H. Li, Y. Zhou, Y. Cao, Z. Sun, Q. Xie, Online monitoring of lithium-ion battery impedance using DC–DC converter self-excited switching oscillations, IEEE Trans. Ind. Electron. (2023) 1–12, http://dx.doi.org/10.1109/TIE.2023.3317850.

[108] B. Liebhart, L. Komsiyska, C. Endisch, Passive impedance spectroscopy for monitoring lithium-ion battery cells during vehicle operation, J. Power Sources 449 (2020) 227297, http://dx.doi.org/10.1016/j.jpowsour.2019.227297.

[109] H. Piret, N. Sockeel, V. Heiries, P.-H. Michel, M. Ranieri, V. Cattin, N. Guillet, P. Granjon, Passive and active tracking of electrochemical impedance of a drone battery, in: EEVC 2015 - European Battery, Hybrid and Fuel Cell Electric Vehicle Congress, 2015, URL https://hal.science/hal-01244009.

[110] S. Buller, J. Walter, E. Karden, R.W. de Doncker, Impedance-based online monitoring of automotive batteries, in: International Advanced Automotive Battery Conference, Vol. 2, 2002, URL https://www.tib.eu/de/suchen/id/BLCP%3ACN072848858.

[111] R.S. Robinson, System noise as a signal source for impedance measurements on batteries connected to operating equipment, J. Power Sources 42 (3) (1993) 381–388, http://dx.doi.org/10.1016/0378-7753(93)90005-L.

[112] L. Raijmakers, EIS data of EiG ePLB C020B; unpublished data, 2014.

[113] L. Raijmakers, EIS data of QinetiQ cell used in 3Ccar H2020 project; unpublished data, 2016.

[114] M.S. Hosen, R. Gopalakrishnan, T. Kalogiannis, J. Jaguemont, J. van Mierlo, M. Berecibar, Impact of relaxation time on electrochemical impedance spectroscopy characterization of the most common lithium battery technologies–experimental study and chemistry-neutral modeling, World Electr. Veh. J. 12 (2) (2021) 77, http://dx.doi.org/10.3390/wevj12020077.

[115] A. Fly, I. Kirkpatrick, R. Chen, Supplementary data for: Low temperature performance evaluation of electrochemical energy storage technologies, 2021, http://dx.doi.org/10.17028/rd.lboro.12662330.v1.

[116] A. Fly, B. Senake-Ralalage, I. Bin-Mat-Arishad, M. Sarmiento-Carnevali, Underlying data: Temperature dependency of diagnostic methods in lithium-ion batteries, 2022, http://dx.doi.org/10.17028/rd.lboro.14883903.v1.

[117] H.S. Chan, E. Dickinson, E. Fedorovskaya, M. Gaberšček, T.P. Heins, N. Meddings, Y.Y. Lee, J. Moškon, J. Park, V. Ruiz, S. Seitz, LiBforSecUse data release - impedance spectra of life cycle tests of commercial 18650 cells, 2022, http://dx.doi.org/10.5281/zenodo.6418665, Zenodo dataset, Version V2.

[118] J. Zhu, Y. Wang, Y. Huang, R.B. Gopaluni, Y. Cao, M. Heere, M.J. Mühlbauer, L. Mereacre, H. Dai, X. Liu, A. Senyshyn, X. Wei, M. Knapp, H. Ehrenberg, Data-driven capacity estimation of commercial lithium-ion batteries from voltage relaxation, 2022, http://dx.doi.org/10.5281/zenodo.6405084, Zenodo dataset, Version v2.

[119] P. Gasper, A. Schiek, K. Smith, Y. Shimonishi, S. Yoshida, Predicting battery capacity from impedance at varying temperature and state of charge using machine learning, Cell Rep. Phys. Sci. 3 (12) (2022) http://dx.doi.org/10.1016/j.xcrp.2022.101184.

[120] M. Rashid, M. Faraji-Niri, J. Sansom, M. Sheikh, D. Widanage, J. Marco, Dataset for rapid state of health estimation of lithium batteries using EIS and machine learning: Training and validation, Data Brief 48 (2023) 109157, http://dx.doi.org/10.1016/j.dib.2023.109157.

[121] T. Rüther, M. Schamel, C. Plank, F. Schomburg, F. Röder, M.A. Danzer, Cell-to-cell-variations of a panasonic NCR18650B, 2023, http://dx.doi.org/10.5281/zenodo.8369275, Zenodo dataset, Version 1.0.

[122] M. Ströbel, V. Kumar, K.P. Birke, Temperature estimation in lithium-ion cells assembled in series-parallel circuits using an artificial neural network based on impedance data, Batteries 9 (9) (2023) 458, http://dx.doi.org/10.3390/batteries9090458.

[123] A. Blömeke, O. Kappelhoff, D.U. Sauer, EIS Data Analytics : v0.0.9, RWTH Publications, 2024, http://dx.doi.org/10.18154/RWTH-2024-03849.

[124] H.L. Laufen, S. Klick, H. Ditler, K.L. Quade, A. Mikitisin, A. Blömeke, M.F. Schütte, D. Wasylowski, M. Sonnet, L.A.J. Henrich, A. Schwedt, G. Stahl, F. Ringbeck, J. Mayer, D.U. Sauer, Data: Multi-method Characterization of a Commercial 1.2 Ah Sodium-Ion Battery CellIndicates Drop-in Potential, RWTH Publications, 2024, http://dx.doi.org/10.18154/RWTH-2024-04088.

[125] M. Luh, T. Blank, Addendum to "comprehensive battery aging dataset: Capacity and impedance fade measurements of a lithium-ion NMC/C-SiO cell, 2024, http://dx.doi.org/10.35097/krk531nmj4bsshha.

[126] Houssam. Rabab, Modeling of Sodium-Ion Batteries for On-Board Diagnosis of Their States of Charge and Health (Ph.D. thesis), Universit'e de technologie de Compi'egne, 2024, http://dx.doi.org/10.13140/RG.2.2.16024.61448.

[127] H. Mustafa, C. Bourelly, M. Vitelli, F. Milano, M. Molinara, L. Ferrigno, SoC estimation on Li-ion batteries: A new EIS-based dataset for data–driven applications, 2024, http://dx.doi.org/10.17632/cb887gkmxw.2, Mendeley dataset, Version 2.

[128] S. Fasolato, N. Blasuttigh, G. Galuppini, D.M. Raimondo, A dataset for large prismatic lithium-ion battery cells (CALB L148N58A): Comprehensive characterization and real-world driving cycles, Data Brief 58 (2025) 111301, http://dx.doi.org/10.1016/j.dib.2025.111301.

[129] K. Yang, Z. Feng, Y. Zhu, Y. Zhang, B. Feng, Z. Song, J. Meng, Uncertainty characterization of rapid battery impedance measurements using binary sequence, J. Energy Storage 131 (2025) 117617, http://dx.doi.org/10.1016/j.est.2025.117617.

[130] C.G.T. Inc., Iceberg 3.0 - A highly scalable enterprise platform for automotive benchmarking, 2025, URL https://www.caresoftglobal.com/. (Accessed 18 November 2025).

[131] E. Engineering, What is the slot/pole combination of main EV/HEV e-powertrains? 2022, URL https://web.archive.org/web/20220528015857/https://eomys.com/e-nvh/technical-notes-on-electromagnetically-excited-noise-and-vibrations/article/what-is-the-slot-pole-combination-of-main-ev-hev-e-powertrains. (Accessed 18 November 2025).

[132] D. OTAKU, 47kW electric car motor from MITSUBISHI i-MiEV. [Eng sub], 2021, URL https://www.youtube.com/watch?v=r_M7hxoIePg. (Accessed 18 November 2025).

[133] M. Live, Ford mach-E rear motor teardown and analysis, 2021, URL https://www.youtube.com/watch?v=mHVV52lPyIs&list=PLkiDlGyJnprdm1Jw35ZSTKbTa3CDoAHmn&index=4. (Accessed 18 November 2025).

[134] M. Live, A multitude of motors | rivian R1T electric drive unit, 2022, URL https://www.youtube.com/watch?v=Ldw5w3x5kUc&list=PLkiDlGyJnprdm1Jw35ZSTKbTa3CDoAHmn&index=6. (Accessed 18 November 2025).

[135] M. Live, Tesla cybertruck 845-HP "Cyberbeast" motors!, 2024, URL https://www.youtube.com/watch?v=MfJip4JUljg&list=PLkiDlGyJnprdm1Jw35ZSTKbTa3CDoAHmn&index=12. (Accessed 18 November 2025).

[136] M. Live, Tesla model S plaid motor EXTRAVAGANZA!!, 2022, URL https://www.youtube.com/watch?v=4lGVimLK58g&list=PLkiDlGyJnprdm1Jw35ZSTKbTa3CDoAHmn&index=5. (Accessed 18 November 2025).